

Research Programme of the Research Fund for Coal and Steel

STRONGer Steels in the Built Environment (STROBE)

D2.3 - Numerical simulation program on beams

Markus Feldmann, Helen Bartsch, Felix Eyben, Simon Schaffrath
RWTH Aachen University



Institute of
Steel Construction

RWTHAACHEN
UNIVERSITY

WP 2 – Plastic Design with HSS

Deliverable 2.3

RFSR-CT-2016-743504

STROBE

Version	Date	Purpose	Author	Reviewer	Approved
01	21/06/2019	First Version	Bartsch		
02	18/01/2021	Second Version	Eyben/ Bartsch		
03	03/02/2021	Third Version	Eyben/ Bartsch	Schaffrath	

EXECUTIVE SUMMARY

Within the scope of the STROBE project, investigations on the rotational capacity were carried out. Both homogeneous beams made of high-strength steel (HSS) and hybrid steel beams were experimentally tested with regard to their rotation capacity.

This report deals with the numerical simulations of beams made of HSS. For the numerical simulations, a python script has been designed in order to vary beam characteristics, such as geometry and material, in a simple way.

First, the experimental investigations were modelled. Here, the true stress-strain curves of WP1 were incorporated, as well as the damage criterion. A good agreement was obtained between the experimental results in terms of moment-rotation curve, deformations and also crack initiation and growth. Thereby, the FE model is verified.

Second, a large numerical parametric study has been conducted in order to investigate the main influences on rotation capacity of the beams. 24 true stress-strain curves have been taken into account together with 6 damage curves, referring to different upper-shelf toughness levels. S690 as well as S500 materials have been taken into account, as well as hybrid beams made of combinations of S690, S500 and S355.

Slenderness of flange and web, thickness and width of flange and web as well as different length of the beams have been varied. Additionally, the influence of imperfection size, lateral support, stiffeners and loading conditions are assessed.

To sum up, the numerical study has shown that HSS can have sufficient rotation capacity for plastic design, depending on various factors. The results gained during the investigations presented here serve to defined design recommendations, described in Deliverable 2.5.

Table of Contents

1	Introduction	1
2	Numerical simulation of experimental investigations	2
2.1	Development of FE model	2
2.1.1	Geometry	2
2.1.2	Loading and boundary condition	2
2.1.3	Discretisation	3
2.1.4	Material	3
2.2	Modelling the tests	5
2.2.1	Buckling analysis	5
2.2.2	Load bearing analysis	6
3	Influences on rotation capacity of beams	10
3.1	Rotation capacity depending on section slenderness and material characteristics	10
3.1.1	Material properties	10
3.1.2	Cross sections	13
3.1.3	Results	15
3.2	Rotation capacity depending on hybrid sections, length, boundary conditions and loading	26
3.2.1	Buckle eigenform	26
3.2.2	Imperfection size	28
3.2.3	Beam length	29
3.2.4	Stiffness of lateral support	32
3.2.5	Application of stiffeners	34
3.2.6	Hybrid beams	35
3.2.7	Loading condition	38
4	Summary	43
5	References	45
6	Annex: Moment-Rotation diagrams	46

1 INTRODUCTION

Today, the production of high-strength steels is an economical alternative to conventional steels.. The comparatively higher strengths result in improved cross-sectional load-bearing capacities and therefore smaller cross-sections can be selected for the same load-bearing capacity. This achievement makes it possible to build slender structures and thus significantly reduce weight. This holds considerable potential from a technological and ecological point of view.

Plastic design allows the utilisation of load-bearing reserves and represents a possibility for the economic dimensioning of structures. A fully plastic moment redistribution and sufficient rotation capacity are assumed. However, this design concept has so far only been permitted in European standards for compact cross-sections up to a steel grade of S460. High-strength steels are excluded from this design concept due to their lower ductility.

Previous investigations [1] [2] show that components made of high-strength steel are also capable of applying the plastic moment capacity and, with correspondingly compact cross-sections, have sufficient rotational capacity. The requirements for a plastic design can therefore also be met when using high-strength components. The approval of the application of this design method would be associated with a considerable increase in the economic efficiency of steel structures.

Within the scope of the STROBE project, further investigations on the rotational capacity were carried out. Both homogeneous beams made of conventional strength steel and high-strength steel as well as hybrid steel beams were experimentally tested with regard to their rotation capacity, see Deliverable 2.1.

The following sections give information on the validation of the numerical models and the influences of several aspects on the rotation capacity of HSS beams.

2 NUMERICAL SIMULATION OF EXPERIMENTAL INVESTIGATIONS

The simulations of I-girders under moment-rotation loading situations are realised with the finite element (FE) program ABAQUS 6.14, as explained in the following sections.

2.1 Development of FE model

The model development has been realised by scripting a python file, where input parameters regarding geometry, material, presence of stiffeners and model and mesh settings can be easily changed. The script is then imported into ABAQUS and multiple models can be created within minutes.

2.1.1 Geometry

The geometry of the model is limited to I-beams with variable span, which are composed of different components that can be adapted in their dimensions: flanges, web, longitudinal welds, vertical stiffeners at the load introduction and supports (optional), welds at the stiffeners. Figure 1 depicts the geometry of an exemplary numerical model.

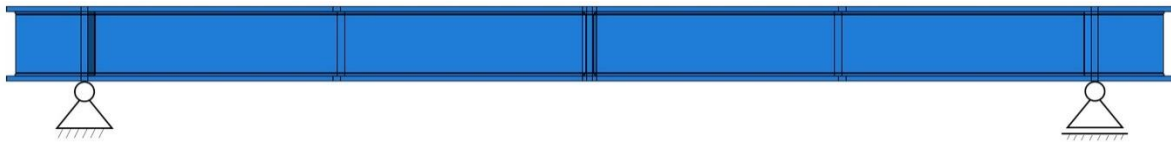


Figure 1: Depiction of numerical model for rotation investigations on beams

2.1.2 Loading and boundary condition

The vertical load is applied via a reference point in the middle of the beam, which is coupled with the upper flange over its entire width. The width of the load introduction corresponds in a simplified way to the thickness of the stiffener. The model provides for two vertical supports, the position of which is specified by the span. The support width corresponds to the thickness of the stiffener in a simplified way. Lateral supports can be considered to avoid torsional flexural buckling. The distance to the load introduction and the supports can be varied. The width of the lateral support is variable, the height is fixed by the flange thickness. It is possible to adopt the lateral supports rigidly or to provide them with a spring stiffness, so that a lateral deflection of the beam is permitted to a certain extent. The springs are designed to apply only compressive forces, in accordance with the experimental tests. In addition, the beam is prevented from lateral deflection at the point of load introduction.

Figure 2 exemplarily illustrates the lateral supports in the form of springs for a long test specimen.

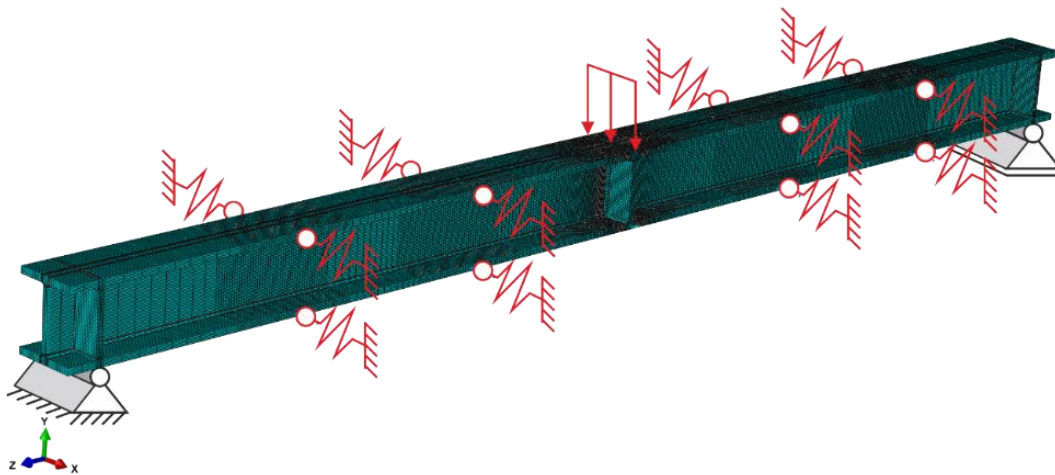


Figure 2: Depiction of meshed “long” beam with lateral supports in the form of springs

2.1.3 Discretisation

The discretisation is specified by a combination of a globally defined element size and locally adapted element sizes. Thus, the different areas and components of the beam can have different element sizes. This creates a coarse mesh in the outer area and the smaller number of elements improves the calculation time. Areas closer to the beam middle, where plastic deformations and crack initiations occur, consist of smaller elements to improve the accuracy of the results, see Figure 3.

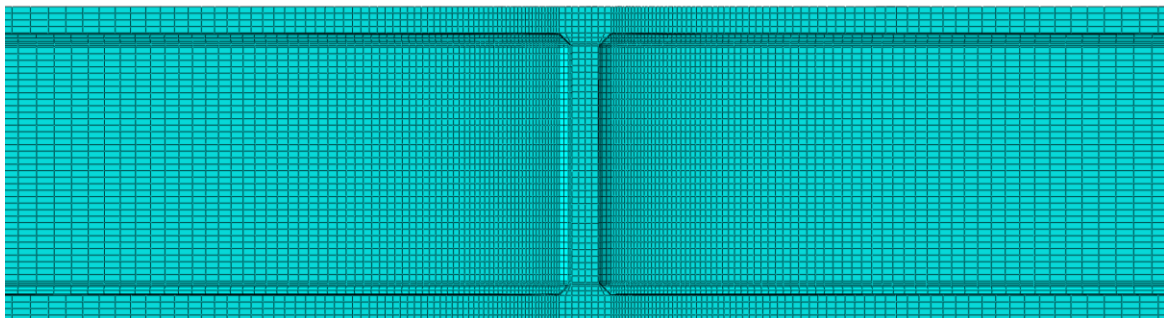


Figure 3: Depiction of discretization of typical numerical model

In doing so, a typical numerical model consists of about 200 000 elements.

2.1.4 Material

Since the plastic behaviour of beams is investigated, material definitions play a huge role. The elastic material behaviour is defined by a Young’s modulus of 210 000 MPa and a Poisson’s ratio of 0.3. However, the definition of the plastic material characteristics in terms of true stress strain curves, also called flow curves, is more complex.

A valuable approach to describe flow curves is the procedure of Ludwik [3] and Hollomon [4], which was adapted by Schaffrath [5]. The function of the flow curve is defined section by section as follows, see also Deliverable D1.1.

$$\sigma_w = \begin{cases} \frac{\sigma_{w,0}}{(1 - 0,5 \cdot \varepsilon_w)^2} & \text{for } \varepsilon_w \leq \Delta\varepsilon_{w,l} \\ \frac{\sigma_{w,0}}{(1 - 0,5 \cdot \Delta\varepsilon_{w,l})^2} + k_L \cdot (\varepsilon_w - \Delta\varepsilon_{w,l})^{n_L} & \text{for } \varepsilon_w > \Delta\varepsilon_{w,l} \end{cases} \quad (1)$$

with:

$$n_L = \frac{\sigma_{w,u} \cdot (\varepsilon_{w,u} - \Delta\varepsilon_{w,l})}{\sigma_{w,u} - \frac{\sigma_{w,0}}{(1 - 0,5 \cdot \Delta\varepsilon_{w,l})^2}} \quad (2)$$

$$k_L = \frac{\sigma_{w,u} - \frac{\sigma_{w,0}}{(1 - 0,5 \cdot \Delta\varepsilon_{w,l})^2}}{(\varepsilon_w - \Delta\varepsilon_{w,l})^{n_L}} \quad (3)$$

where σ_w ist the true stress, ε_w is the true strain, $\sigma_{w,0}$ depicts the yield stress, $\Delta\varepsilon_{w,l}$ depicts the strain hardening strain, n_L and k_L are parameters of the function and $\sigma_{w,u}$ depicts the true stress at load maximum and $\varepsilon_{w,u}$ is the true strain at load maximum. These flow curve parameters can directly be calculated out of the three points of a technical (engineering) stress strain curve yield strength f_y , tensile strength f_u and ultimate elongation ε_u .

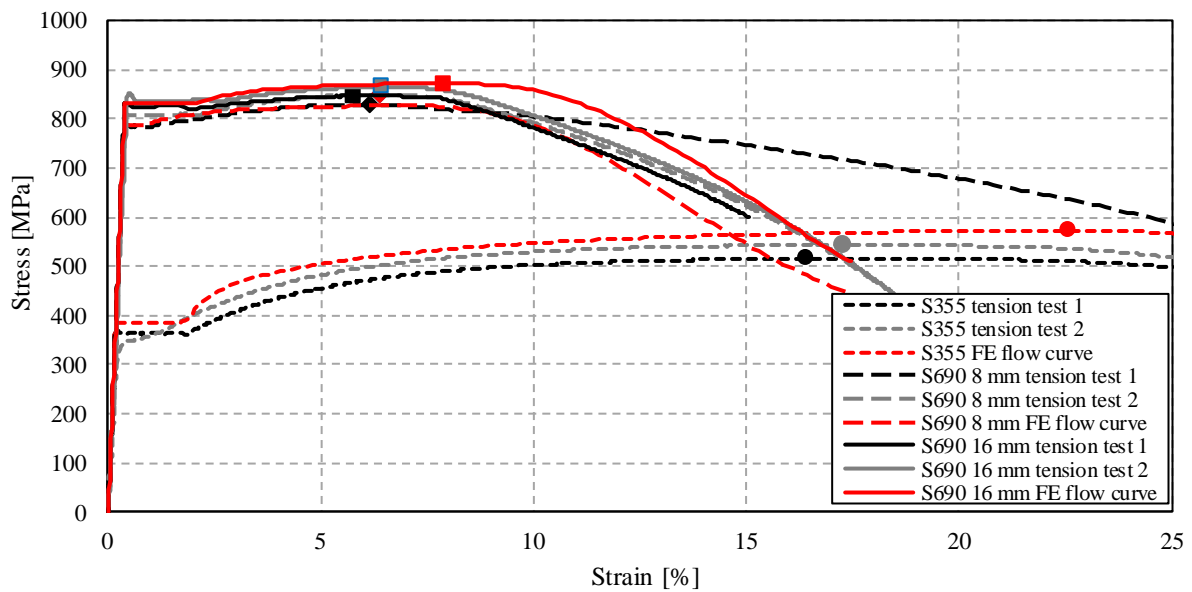


Figure 4: Comparison of experimental and numerical tensile tests results using an adjusted flow curve in case of all 3 utilised materials

Regarding definition of flow curves, different approaches have been applied for modelling the tests and investigating general influencing factors in the frame of a case. For the modelling of the tests, firstly tensile test of the actual material of the specimens have been conducted. Next, with the help of equation (1), an initial flow curve is described, based on results of two independently conducted tensile tests series. This flow curve is adjusted slightly to fit all test results of the large-scale tests. Figure 4 presents the comparison of experimentally and numerically derived stress-strain curves using finally adjusted flow curves.

However, for the case study investigating various influencing factors on rotation capacity of HSS beams, nominal material characteristics should be considered in order to derive design recommendations. The material characteristics are based on nominal flow curves and nominal damage curves, described in Deliverable D1.1.

2.2 Modelling the tests

In the experimental test program to determine the rotational capacity of high-strength beams, twenty test specimens with double-symmetric I-sections were tested for their rotational behaviour, see also Deliverable D2.1. These tests are modelled numerically in order to validate the FE model in a first step, as explained in the following sections.

2.2.1 Buckling analysis

First, an elastic buckling analysis is conducted in order to investigate eigenmodes of the specimens. The first relevant eigenmode displaying local buckling is then used to define imperfections for the load bearing analysis. During imperfection measurements, a maximum imperfection of 1 mm has been determined, see Deliverable D2.1. Therefore, the first positive eigenmode is modelled as an imperfection with a maximum ordinate of 1 mm. Figure 5 illustrates a result of a typical eigenmode analysis.

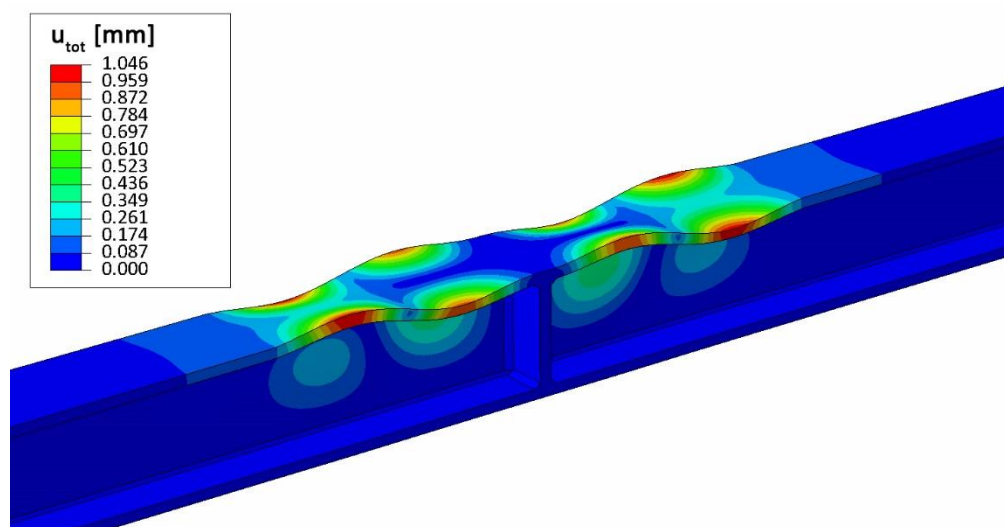


Figure 5: First eigenmode of typical beam model

2.2.2 Load bearing analysis

In the load bearing analysis, a three-point bending test is simulated on the specified beam with the previously determined imperfection. The deformation is applied in the centre of the beam with displacement control, as measured from the experimental tests.

The deformation figure of the beam showed similar buckling as the given buckling shape, as Figure 6 shows for the beams S101, S103 and S110 of the component tests.

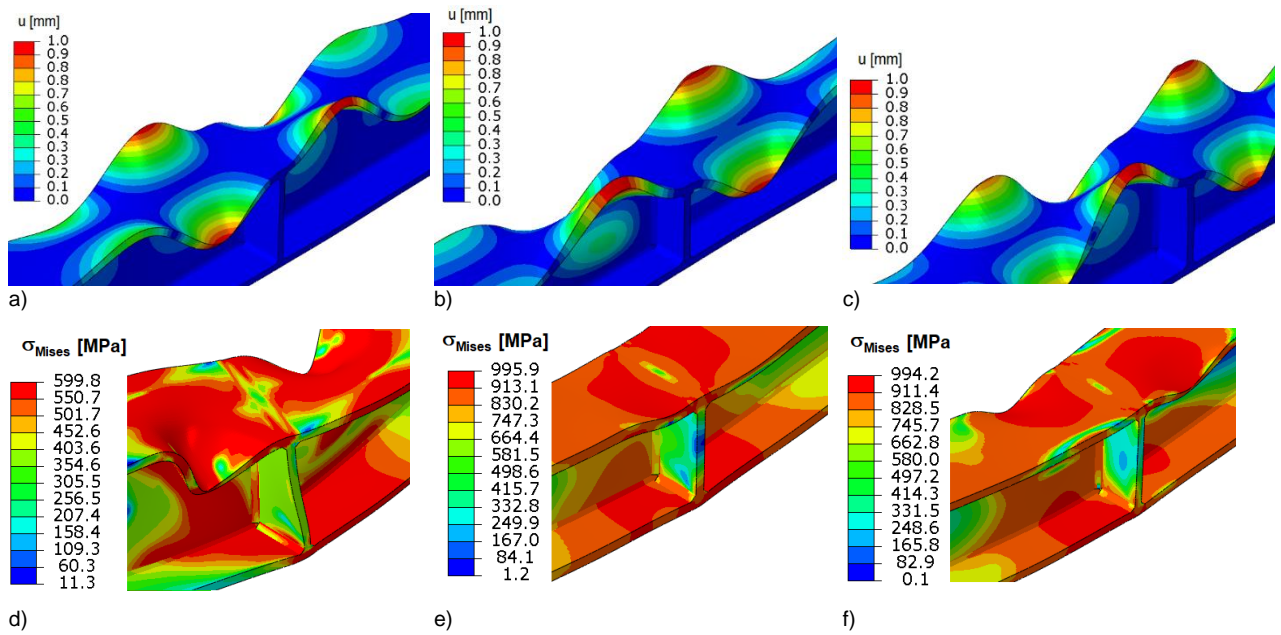


Figure 6: Comparison of deformation figures in buckling analysis (scale factor 100) of a) S101 (no lat. support) b) S103 (2 lat. supports) and c) S110 (4 lat. supports) and load bearing analysis of specimen of d) S101, e) S103 and f) S110

All measurements recorded during the tests as displacement and force in the middle of the section, rotations at the beam ends and strains in top and bottom flange are also evaluated in the simulations in order to compare results as accurate as possible.

As explained in section 2.1.4, the flow curves of the three materials have been slightly adjusted to the test results in order to achieve a good agreement between test and simulations. Due to material changes in the heat affected zone at the stiffener, slight deviations of flow curves in component and small-scale tests have to be accepted. Only one flow curve per material is used in all simulations of beams consisting of the respective material.

In order to be able to also reproduce the crack initiation of some beams during the experimental tests, 2D damage curves, as explained in Deliverable D1.1, are calibrated according to Johnson-Cook [6]. For this purpose, the location where crack initiation started in the test was noted for all beams of the experimental investigations where failure occurred due to crack initiation and propagation. The numerical simulation was evaluated with regard to the stress triaxiality and the equivalent plastic strain in two elements at the location and time of crack initiation in the test. A 2D

damage curve can be extrapolated from these two pairs of values. First of all, respective damage curves are determined for all beams in which a failure due to crack initiation and crack propagation has occurred. Then a mean damage curve is established to describe the damage of the material on average. The damage curves are incorporated into the simulations by a subroutine. As soon as the plastic failure strain is reached in an element, the subroutine stops the numerical simulation.

Figure 7 illustrates the individually determined damage curves as well as the medium damage curves.

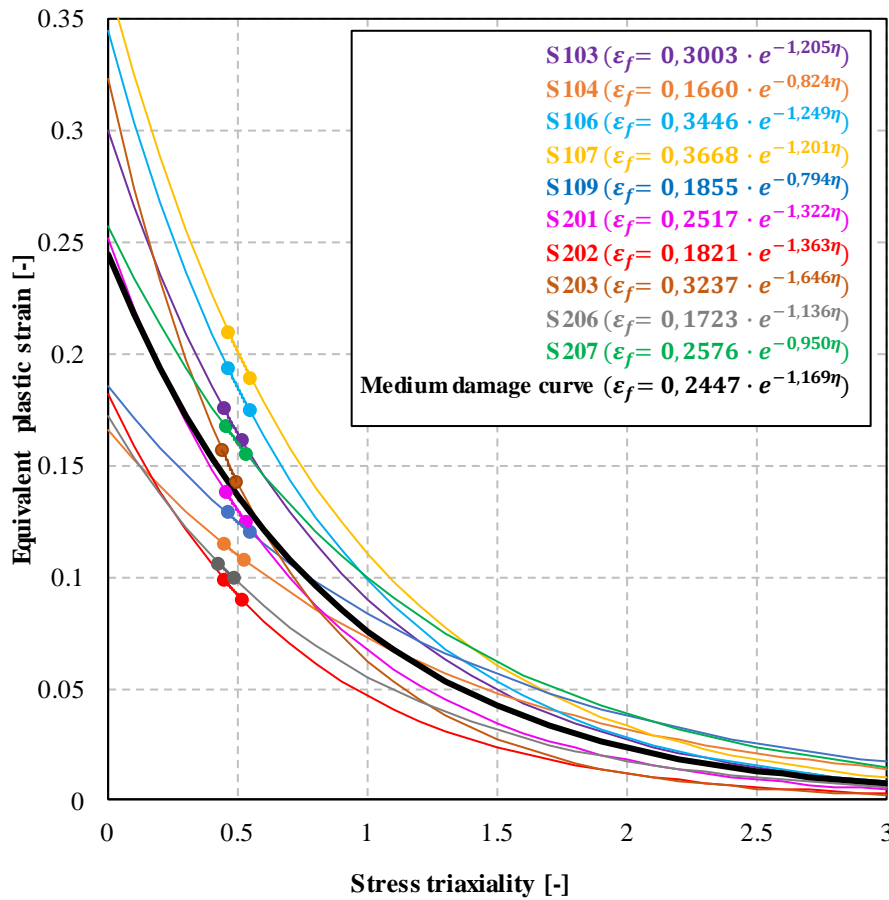


Figure 7: Individually determined damage curves of all beams whose failure was characterised by crack initiation and propagation, and the mean damage curve

It becomes evident, that all failed beams lie within a similar stress triaxiality range and that there is a considerable scatter in the failure strain. Generally, for each material a separate damage curve should be applied. In this case however, all failures occurred in one material (S690, 16 mm), so that only one flow curve is relevant.

Figure 8 and Figure 9 present the comparison of experiment and simulation using individual and the mean damage curve for two specimens. First, it can be seen that the general moment-rotation progression can be depicted very well. The numerical model including the flow curves is capable of depicting the plastic material behaviour very well. Moreover, the usage of individual damage

curves leads to an accurate prediction of failure, as seen in Figure 8. Here, the experiment can be simulated very precisely. However, since only one damage curve should be applied to all specimens, the simulations using the mean damage curve have to be regarded, as presented exemplarily in Figure 9. The time of damage is in some cases over and in some other underestimated, since the mean damage curve has been applied. The location of damage is always simulated correctly in the tension flange near the stiffener, see Figure 10.

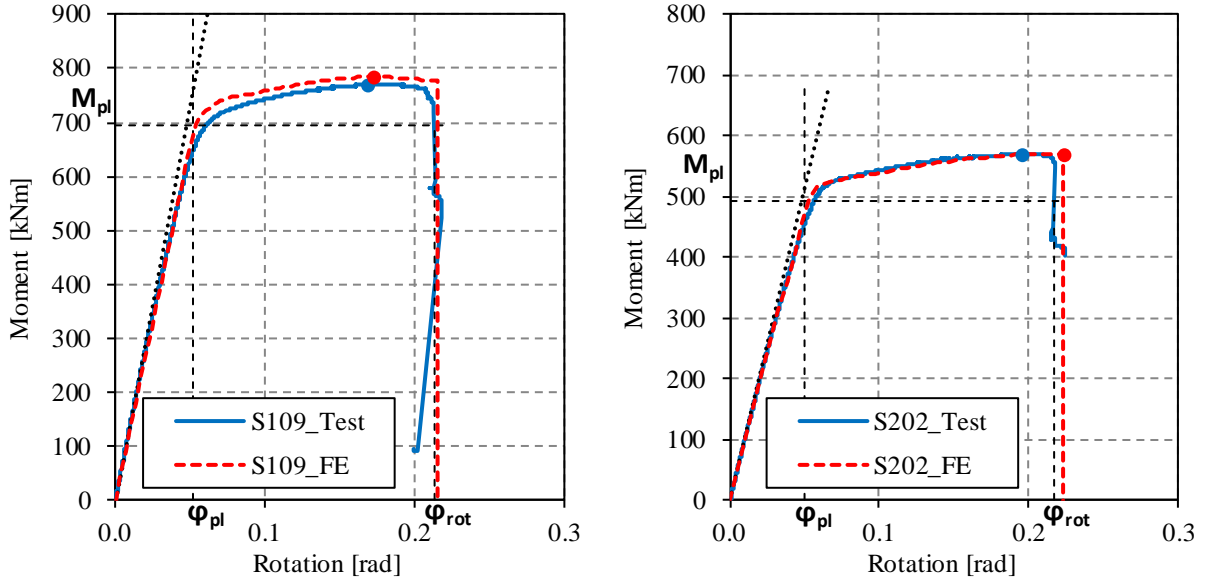


Figure 8: Validation of the individual damage curves on beams S109 (left) and S202 (right)

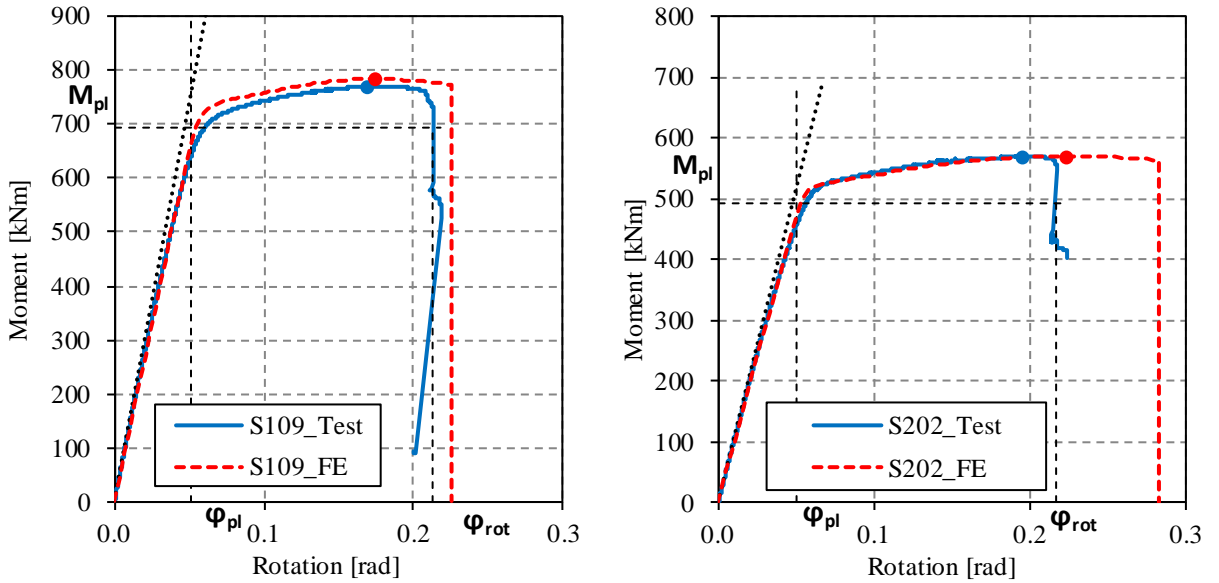


Figure 9: Validation of the mean damage curve on the beams S109 (left) and S202 (right), whose failure was expressed by crack initiation and propagation

The deformation behaviour of test and simulation also showed very good agreements, see exemplarily Figure 11. Apart from comparing moment-rotation curves and damage behaviour, also strain propagations of test and simulation have been considered, see Figure 12. Also here, a good agreement between test and simulation has been observed, while in some cases small over and under estimations in the plastic range occur.

The numerical model is thereby successfully validated.

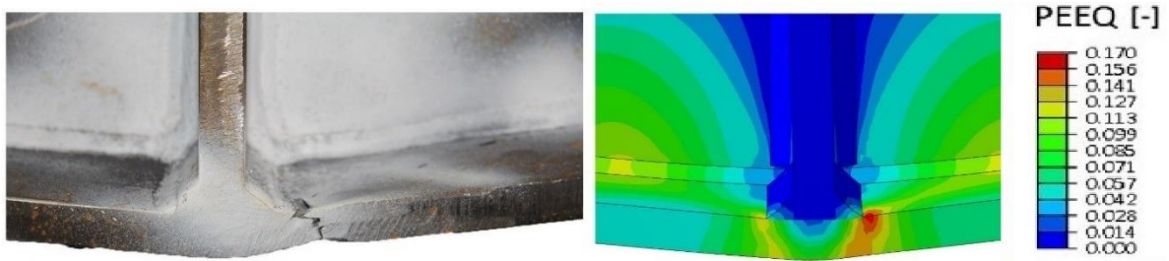


Figure 10: Plastic strains of the numerical simulation at the time of crack initiation compared to the test on beam S103

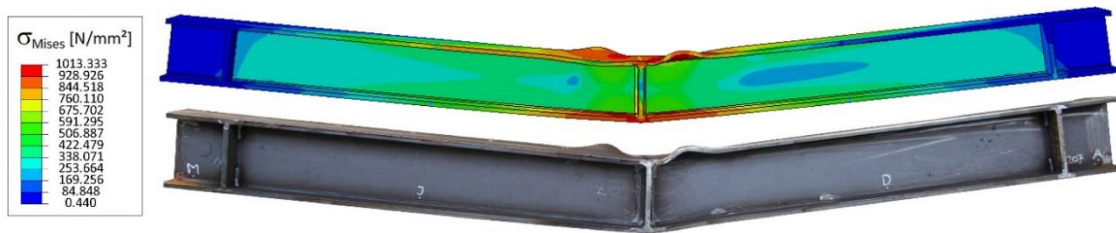


Figure 11: Comparison of the deformation pattern of the beam S207 of the numerical simulation (top) and the experimental deformation pattern (bottom)

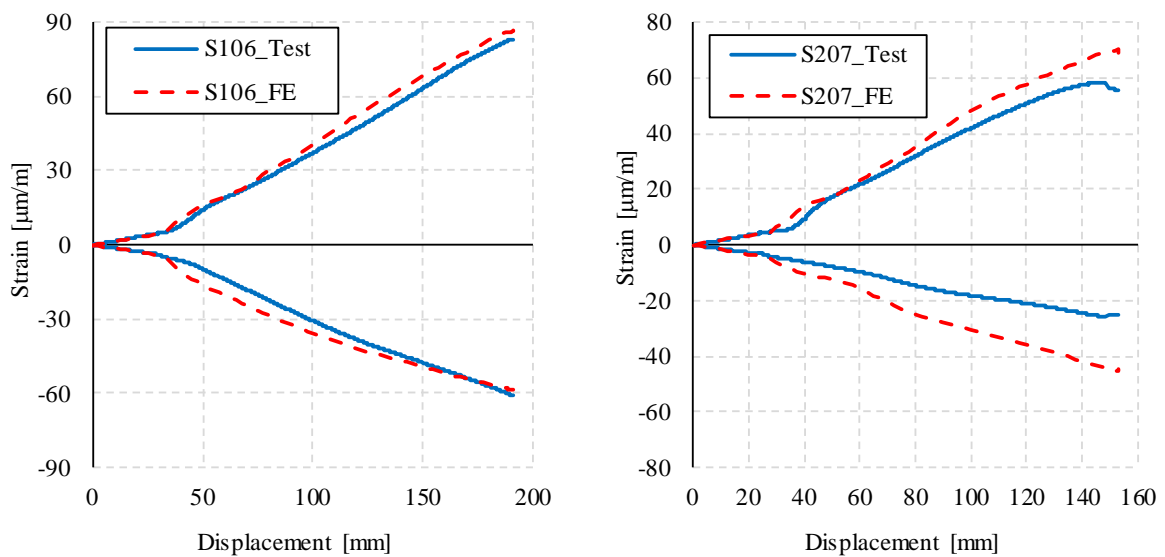


Figure 12: Comparison of numerical and experimental strain progressions of specimens S106 (left) and S207 (right)

3 INFLUENCES ON ROTATION CAPACITY OF BEAMS

After the validation of the numerical models, these can be used in the frame of an extended study investigating different influences on the rotation capacity of homogeneous and hybrid HSS beams. The two main influences on the rotation capacity of beams are the slenderness of the section and the true material characteristics. Additional important parameters are the length to height ratio, boundary conditions and loading scenario. Hybrid sections depict a special case, since two materials have to be considered in terms of material and damage behaviour.

Therefore, in a first main study, the most important factors, slenderness of flange and web and material characteristics of homogeneous beams, have been studied extensively. In a second study, hybrid sections as well as height to length ratio, boundary conditions and loading scenario have been investigated on the basis of selected sections and material characteristics assessed in the main study.

3.1 Rotation capacity depending on section slenderness and material characteristics

3.1.1 Material properties

Since the influences on rotation capacity are analysed in order to derive design recommendations, nominal material parameters are taken into account. These have been derived from a database of actual flow curves as explained in Deliverable D1.1. The flow curve names are equivalent to D1.1, in which the first part is the steel grade, the second part represents the yield ratio, the third part is the uniform elongation and the last part depicts the length of the Lüders-plateau (yield plateau). For the investigations of homogeneous beams, two high strength steels S500 and S690 have been incorporated into the study. For each steel, 24 flow curves with different characteristic yield strength ratio, yield plateau and uniform elongation have been considered. In doing so, all possible configurations of realistic material properties is considered. This way, some of the extreme combinations (e.g. lowest yield ratio with highest uniform elongation) are quite unrealistic, but their individual properties depict possible extreme cases. For each flow curve, a nominal damage curve is also applied in order to consider crack initiation and propagation. The damage curves are also based on a database and have been developed and described in Deliverable D1.1 for a mesh size of 0.06 mm and six different toughness levels (50 to 300 Joule). In addition to these damage curves, a mesh size factor has been evolved for the numerical simulations due to the fact, that the plastic equivalent strain, which is the critical criterion of the damage curves, shows a significant mesh size dependence. To determine a well-founded mesh size factor, the numerical simulations of the experimental test, which have a standard mesh size of 2 mm in the longitudinal direction of the beam, see chapter 2, has been redone with different mesh sizes in the position of the crack initiation. The crack initiation started always right next to the welding in the tension flange

underneath the load application. Because the number of elements used highly increases when choosing a finer mesh size, the submodel-technique was used, see Figure 13. The investigated mesh size varies from 2 mm to 0.06 mm with the intermediate steps 1 mm, 0.5 mm, 0.025 mm. At the time of crack initiation, the plastic equivalent strain and triaxiality was evaluated at the critical point in the corresponding element and afterwards normalized to the results of the mesh size of 0.06 mm. This ensures that the reduction factor for a given damage curve database, with a mesh size of 0.06 mm, is determined.

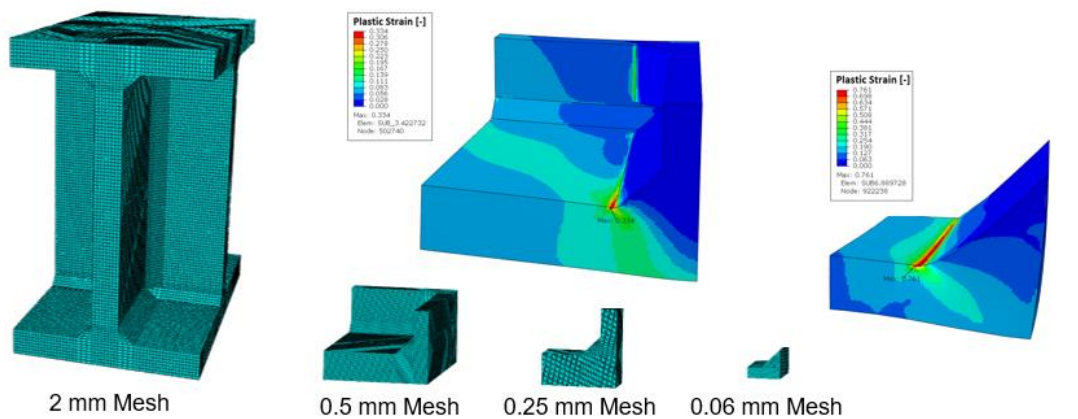


Figure 13: Determination of the mesh size factor – models and submodels with mesh size and plastic equivalent strain

First, the investigations have been done only for cubed elements, which have the same mesh size in all directions. The investigations have then been extended to rectangular elements, which have a small mesh size in the longitudinal direction of the beam and bigger dimensions in the other directions. These rectangular elements should be used in all simulations to reduce the number of elements and thus also the calculation time and requirements for the computing capacity.

In Figure 14, the trend lines for the normalized results with cubed elements for the three beams S201, S107 and S202 from the experimental tests, which represents the upper and lower bounds as well as a mean value from the derivation of the damage curves, see Figure 7, are shown. Furthermore, the result from a predecessor project P950 [7], which dealt with damage mechanics in case of pressure vessel, are shown as comparison. Figure 15 deals with the results for the beam S201, which leads to the lowest (and thus safest) reduction factors in Figure 14, in particular. It can be seen, that for the cubed elements, the relationship can be described very well by an exponential function. The black line represents the true measured values while the orange line is the normalization of the black line to a mesh size of 0.06 mm. For a mesh size of 2 mm in the longitudinal direction, the “+” signs represent the results for rectangular elements, which have a bigger mesh size than 2 mm in the other directions.

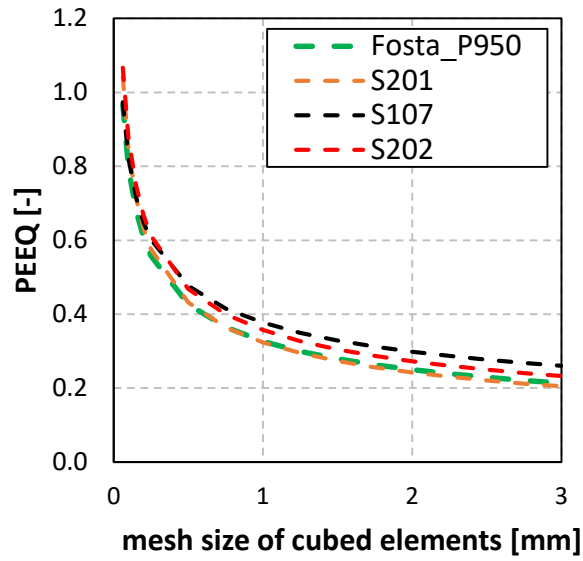


Figure 14: Mesh size versus the plastic equivalent strain for cubed elements for the three beams S201, S107 and S202 from the experimental tests and from an old research project (Fosta P950 [7])

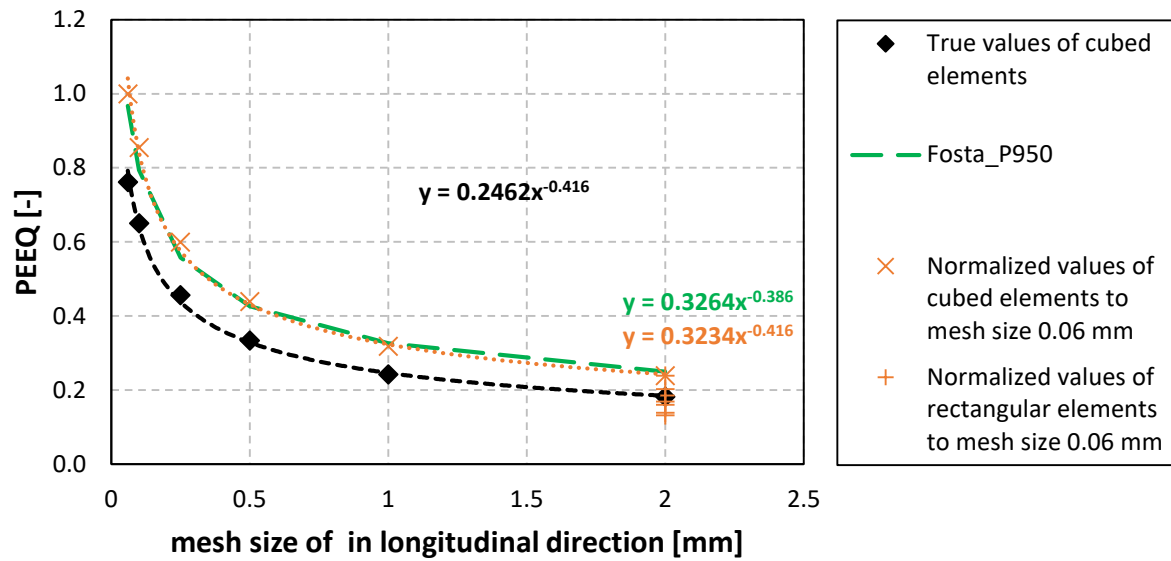


Figure 15: Mesh size versus the plastic equivalent strain for cubed and rectangular elements for the beam S201 and from research project (Fosta P950 [7])

On the safe side, a mesh size factor of 0.17 was chosen based on the results of the beam S201 for a rectangular element with 2 mm in the longitudinal direction and 5 mm in the other two directions, because they are located in the critical area next to the welding of the stiffener under the load application.

3.1.2 Cross sections

The material characteristics are applied to and combined with different sections. These sections have been defined by CSC (cross-section class) definitions according to EC 3-1-1 [8]. Limits of CSC1 are $\frac{c}{t} \leq 9\varepsilon$ for the flange and $\frac{c}{t} \leq 72\varepsilon$ for the web. During the study, the $\frac{c}{t}$ ratios of the flange have been varied by applying $\frac{c}{t} = 4.5\varepsilon$, $\frac{c}{t} = 6.75\varepsilon$ and $\frac{c}{t} = 9\varepsilon$, depicting 50%, 75% and 100% of CSC1 utilisation. Since high slendernesses of the web lead to very high webs with small thicknesses, here four $\frac{c}{t}$ ratios have been investigated: $\frac{c}{t} = 18\varepsilon$, $\frac{c}{t} = 36\varepsilon$, $\frac{c}{t} = 54\varepsilon$ and $\frac{c}{t} = 72\varepsilon$, depicting 25%, 50%, 75% and 100% of CSC1 utilisation. In doing so, the thickness of the flange has been set to 12 mm, while the thickness of the web was 10 mm in all configurations. Weld thicknesses have been calculated on the basis of the plastic moment, while 5 mm was in all cases sufficient. The different slendernesses have been combined with each other, leading to 12 section that have to be investigated for each of the 48 flow curves. In doing so, 576 simulations have been realised.

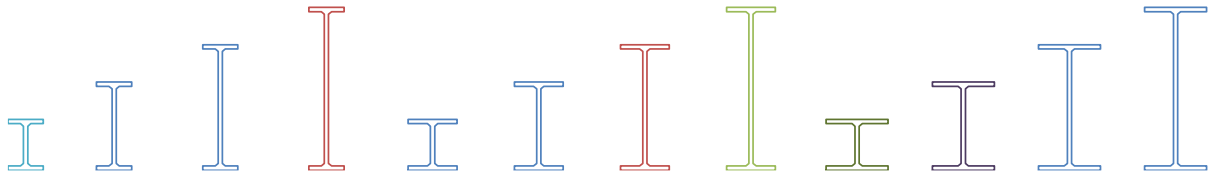


Figure 16: Qualitative depiction of investigated sections for S690

Figure 16 exemplarily depicts the different sections investigated for an S690 cross-section to show the different dimensions.

The analyzed cross section geometries for the average flow curves for the S500 (S500_MW_MW_25) and S690 (S690_MW_MW_25) are listed in Table 1. Here, c/t depicts the slenderness of the part, a_w is the weld thickness, t_{flange} and t_{web} depict the thicknesses of the flange and the web, w_{flange} is the width of the section and h_{web} the height of the web.

Due to the fact that the thicknesses of the flange and the web are constant in the main study, the cross-section classification $c/t\varepsilon$ is constant for one steel grade ($\varepsilon = \sqrt{235/f_y}$) and the cross-section geometries are valid for all investigated flow curves of that steel grade.

Table 1: Cross section geometries used in the main study for the average flow curves for steel grades S500 and S690

	c/t_{flange} [-]	c/t_{web} [-]	a_w [mm]	t_{flange} [mm]	W_{flange} [mm]	t_{web} [mm]	h_{web} [mm]
S500_MW_MW_25	4.50	18.00	5	12	98	10	138
	4.50	36.00	5	12	98	10	261
	4.50	54.00	5	12	98	10	384
	4.50	72.00	5	12	98	10	508
	6.75	18.00	5	12	135	10	138
	6.75	36.00	5	12	135	10	261
	6.75	54.00	5	12	135	10	384
	6.75	72.00	5	12	135	10	508
	9.00	18.00	5	12	172	10	138
	9.00	36.00	5	12	172	10	261
	9.00	54.00	5	12	172	10	384
	9.00	72.00	5	12	172	10	508
S690_MW_MW_25	4.50	18.00	5	12	87	10	119
	4.50	36.00	5	12	87	10	224
	4.50	54.00	5	12	87	10	329
	4.50	72.00	5	12	87	10	434
	6.75	18.00	5	12	119	10	119
	6.75	36.00	5	12	119	10	224
	6.75	54.00	5	12	119	10	329
	6.75	72.00	5	12	119	10	434
	9.00	18.00	5	12	150	10	119
	9.00	36.00	5	12	150	10	224
	9.00	54.00	5	12	150	10	329
	9.00	72.00	5	12	150	10	434

The remaining parameters later on additionally investigated were determined for the main study as follows:

- Span length: 3000 mm
- Stiffeners at supports and load application with thicknesses of flange and including welds
- Lateral supports at six points with a width of 20 times flange thickness and stiff supports in order to achieve efficient calculation times and sizes

3.1.3 Results

In the following, an example evaluation for the average flow curve S690_MW_MW_25 is done. Figure 17 shows the moment-rotation curves for the different slenderness levels. The color of the lines represents the web slenderness (green lines = compact webs, red lines = slender webs) and the lines represent the flange slenderness (solid = compact flanges, dashed = slender flanges).

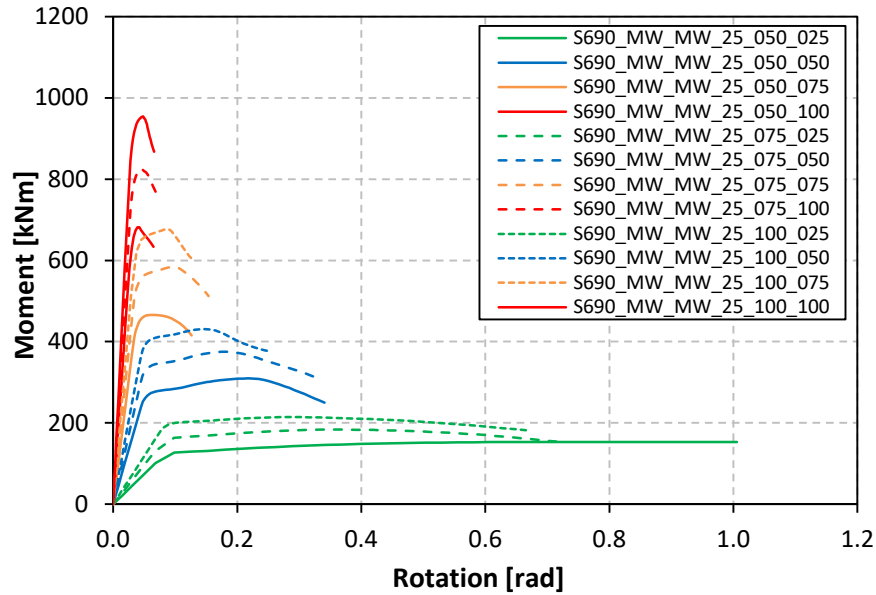


Figure 17: Moment-rotation curves for the different slenderness levels for the average flow curve S690_MW_MW_25 for steel grade S690

All beams were able to reach their individual plastic resistance moment M_{pl} . The diagram shows that the beams made of sections with very slender webs do not rotate strongly compared to the beams made of sections with compact webs. For these curves, the rotation capacity (definition see Deliverable D7.1) was calculated. As explained before, damage curves for six different toughness levels have been applied and lead to different rotation capacities if damage occurred before reaching M_{pl} for the second time. In the diagrams, D1 represents the most conservative damage curve with a toughness level of 50 Joule, D2 equals 100 Joule, D3 150 Joule, D4 200 Joule, D5 250 Joule and D6 represents 300 Joule. The calculated rotation capacities are shown in Figure 18 versus the flange (left) and web (right) slenderness. The colored crosses represent the rotation capacity at the point of crack initiation. It is obvious that the web slenderness (right diagram) shows a big influence on the rotation capacity, while there is no clear trend for the rotation capacity versus the flange slenderness. Crack initiation has an influence on the beams with very compact webs, because as explained before, these beams demonstrate huge rotations on a moment-level beyond M_{pl} . In contrast the beams with very slender webs attain M_{pl} for the second time before damage is predicted by the damage criterion.

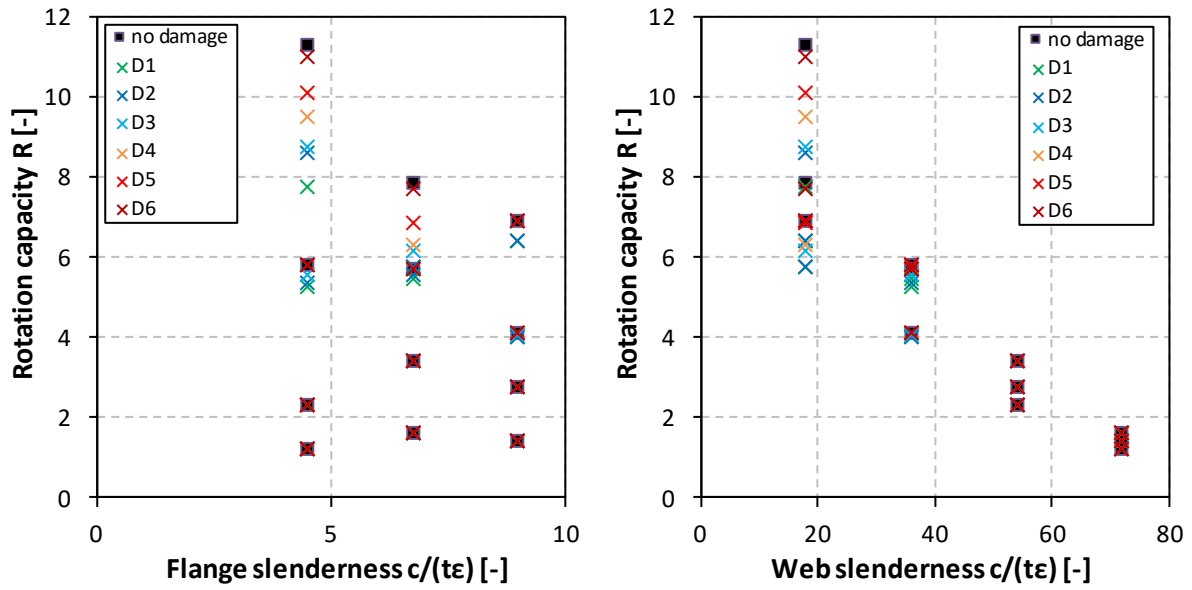


Figure 18: Example evaluation of the twelve different cross sections for the average flow curve S690_MW_MW_25 for steel grade S690

To illustrate the influences in a clear manner, the relevant value of rotation capacity, on the safe side the one referring to toughness level of 50 Joule if damage occurred before reaching M_{pl} for the second time, is presented versus the flange and web slenderness in Figure 19 with a regression surface. Here it is clear to see that the beam with the most compact cross section reached the highest rotation capacity of around 11. No matter how compact the flange is, if the web slenderness is very high (e.g. $c/t\epsilon_{web}=72$) the beams show only small rotation capacities around 1.4.

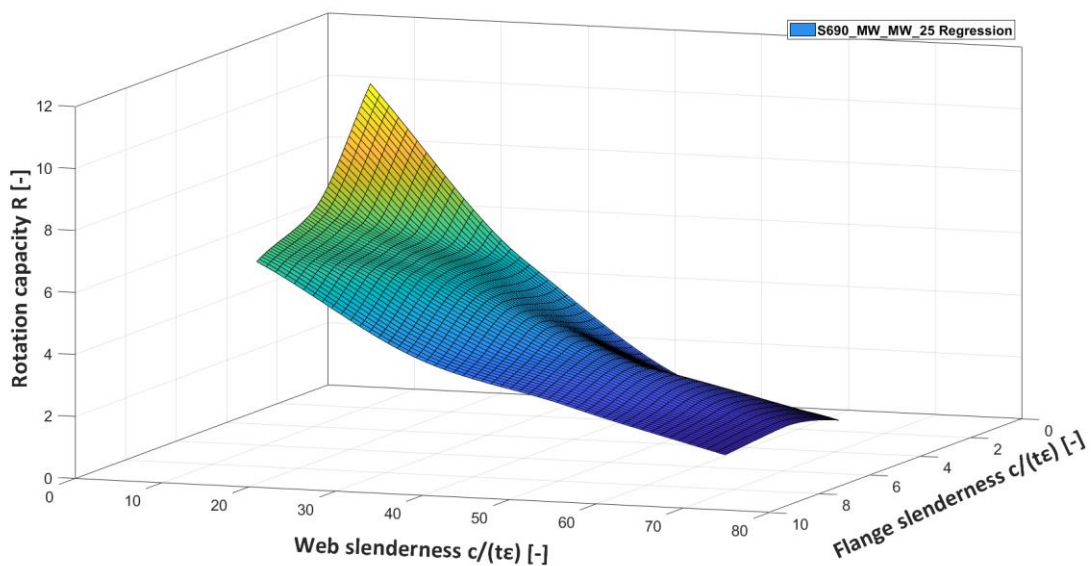


Figure 19: Regression surface for the rotation capacity R as a function of the flange and web slendernesses of the different sections with the average flow curve S690_MW_MW_25 for a steel grade S690

Due to the fact, that the rotation capacity R is strictly related to the absolute rotation angle φ_{rot} , see Deliverable D7.1, the investigations showed similar trends for the different definitions. This is shown in Figure 20 exemplarily for the results for the different sections, related to the web slenderness, for the average flow curve S690_MW_MW_25 for the steel grade S690.

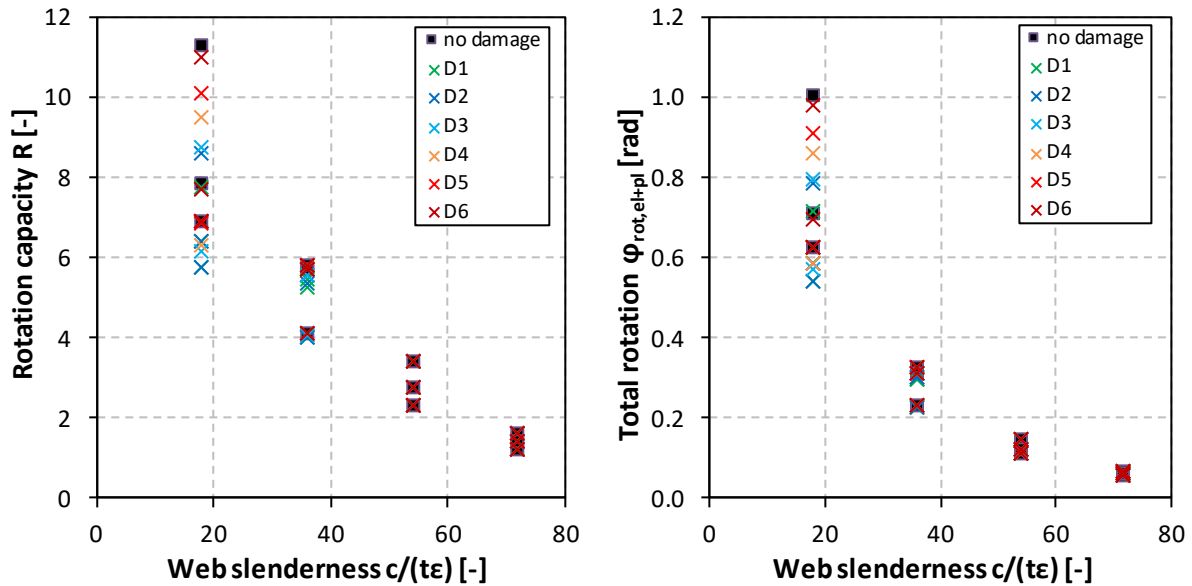


Figure 20: Comparison between evaluation based on rotation capacity (left) and absolute values represented by the plastic rotation angle φ_{rot} (right) for different web slendernesses for the average flowcurve for an S690 (S690_MW_MW_25)

Consequently, all beams are evaluated in the following with regard to their rotation capacity, as this is system-independent and can therefore be used well for comparisons.

The results of the main study for all 576 investigated combinations of slenderness levels and materials are shown in Figure 21, in which the rotation capacity R is depicted against the flange and web slendernesses. The decisive criterion, whether the plastic resistance moment M_{pl} was reached for the second time (blue crosses) or if damaged occurred before that point (black crosses). A reference rotation capacity of $R=3$ is also plotted, which is the given minimum requirement from EC3-1-1 [8].

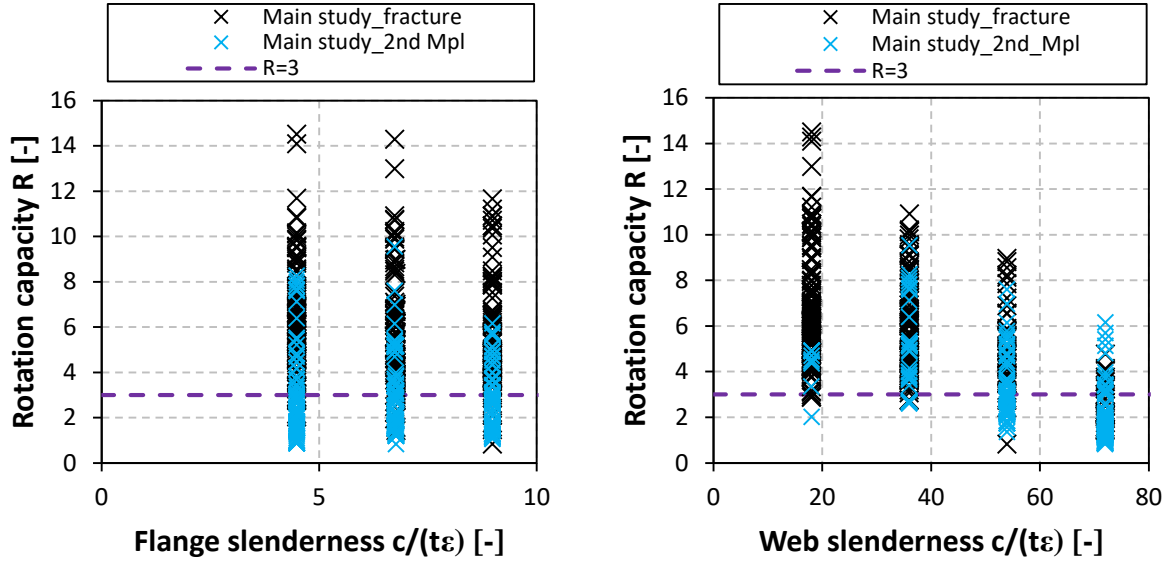


Figure 21: Rotation capacity versus of flange slenderness (left) and web slenderness (right)

All 576 investigated beams were able to reach M_{pl} and to withstand a certain rotation. When analyzing the rotation capacity over the flange slenderness, no clear trend is obvious. For the three investigated flange slendernesses there are cases with high and low rotation capacities. Regarding the web slenderness, it is evident that there is a clear trend that the beams with the higher web slendernesses ($\geq 54 c/t_{\epsilon_{web}}$) tend to have low rotation capacities. When looking at the damage criterion it is obvious that the beams made of sections with very slender webs attain their rotation capacity by reaching the M_{pl} level for the second time, while the beams with compact webs fail due to damage before reaching M_{pl} for the second time. This behaviour is explained with Figure 22.

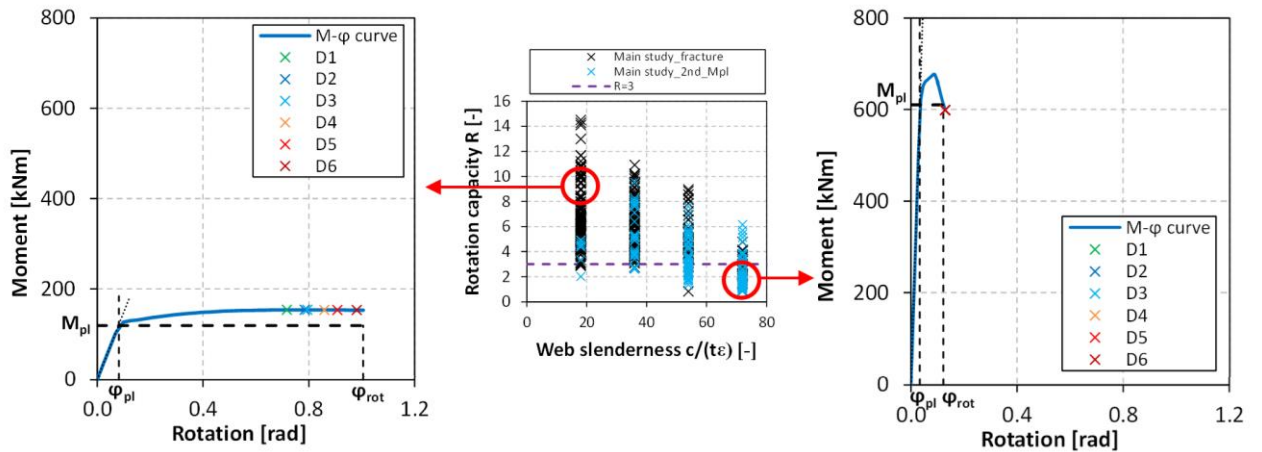


Figure 22: Comparison of failure criterion for a beam with a compact web (left) and a very slender web (right)

The beams with compact webs (left diagram) show huge rotations and achieve a much bigger moment than the analytical resistance moment M_{pl} and damage for all six toughness levels (D1: 50 Joule, D6: 300 Joule) is predicted before reaching M_{pl} for the second time. On the contrary, the beams with very slender webs can withstand lower moments and additionally do not show much rotation. Due to this merely small jump above the plastic resistance moment, damage occurs for all six toughness levels after reaching M_{pl} for the second time.

In addition to the clear influence by (especially) the web slenderness on the rotation capacity, the influence of different material properties, as derived and described in Deliverable D1.1, has been investigated.

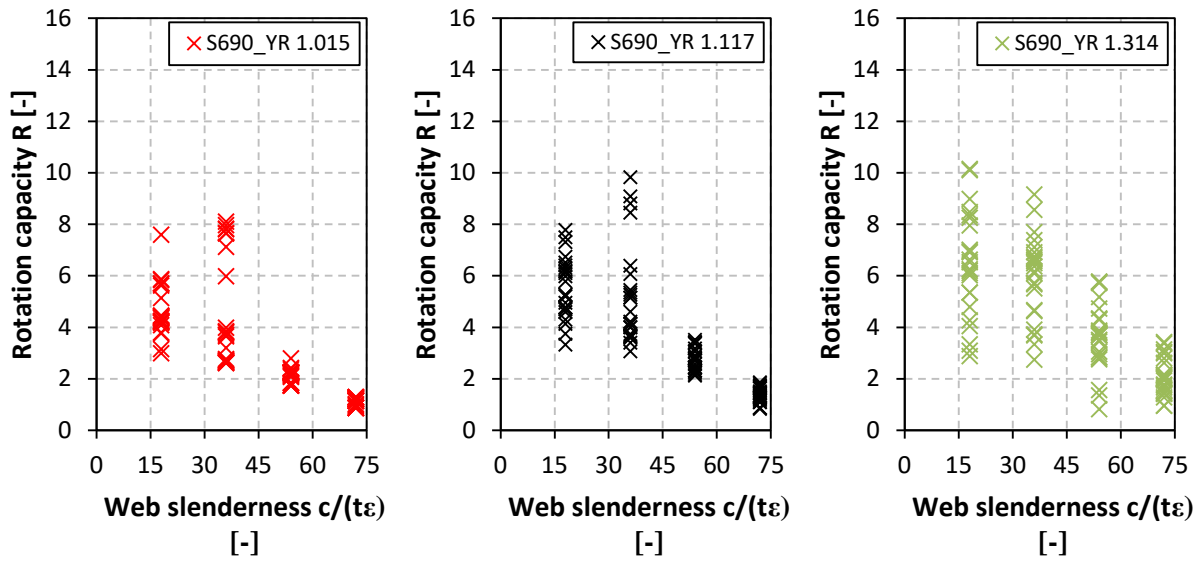


Figure 23: Influence of the three different yield ratios 1.015 (left), 1.117 (middle) and 1.314 (right) versus the web slenderness on rotation capacity of S690 beams

For the steel grade S690, three different yield ratios have been investigated: 1.015, 1.117 and 1.314. Figure 23 depicts the influence of the yield ratio versus the web slenderness for the steel grade S690.

It is obvious, that the slenderness is the most decisive criterion on the rotation capacity. The rotation capacity of beams with a higher yield ratio (right diagram) shows a greater scatter and slightly higher values in the trend than the rotation capacity of beams with a low yield ratio (left diagram). A higher yield ratio is therefore preferable to achieve higher rotations. It is important to mention, that the lowest investigated yield ratio of 1.015 for an S690 does not fulfill the requirements of EN 1993-1-12 [9], which is a yield ratio $f_u/f_y \geq 1.05$. However, in the database for the flow curves of Deliverable D1.1, these values depict the lower bound and have therefore been considered for the numerical study.

The rotation capacity versus the web slenderness and the three investigated uniform elongations for the steel grade S690 (3.6 %, 8.4 % and 13.5 %) is plotted in Figure 24.

Again, the web slenderness has the biggest influence on the rotation capacity. When looking at the beams with slender webs ($c/(t\epsilon)_{web}=72$) no trend is discernible and the rotation capacity is nearly the same for the different uniform elongations. Comparing a uniform elongation of 3.6 % (left diagram) with 8.4 % (middle diagram), the beams with compact webs ($c/(t\epsilon)_{web}=16$) tend to reach higher rotation capacity with a higher uniform elongation. But the beams with a material with even higher uniform elongation (13.5 %, right diagram) do not show a higher rotation capacity. To conclude, the influence of the uniform elongation is marginal and only affects beams with compact sections, which can reach a sufficient rotation on all levels.

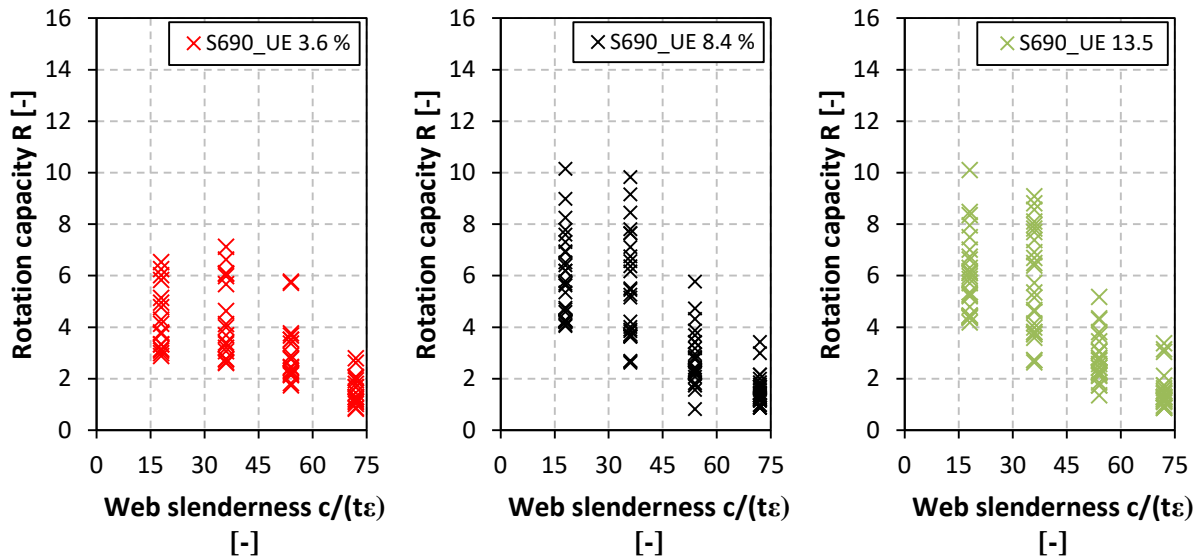


Figure 24: Influence of the three uniform elongations 3.6 % (left), 8.4 % (middle) and 13.5 % (right) versus the web slenderness on rotation capacity of S690 beams

Figure 25 shows the influence of the yield plateau on the rotation capacity of beams made out of S690. As described in Deliverable D1.1, three different levels for yield plateaus (0 %, 2.5 % and 5 %) have been investigated, since no clear trend in the database was obvious.

The influence of the yield plateau on the rotation capacity is small for the S690 beams. There is a slight trend, that for beams with very slender webs a long yield plateau (right diagrams) leads to lower rotation capacities. For beams with compact webs, a higher yield plateau leads to lower rotation capacities. Again, the influence of the web slenderness is much higher than the impact of the yield plateau.

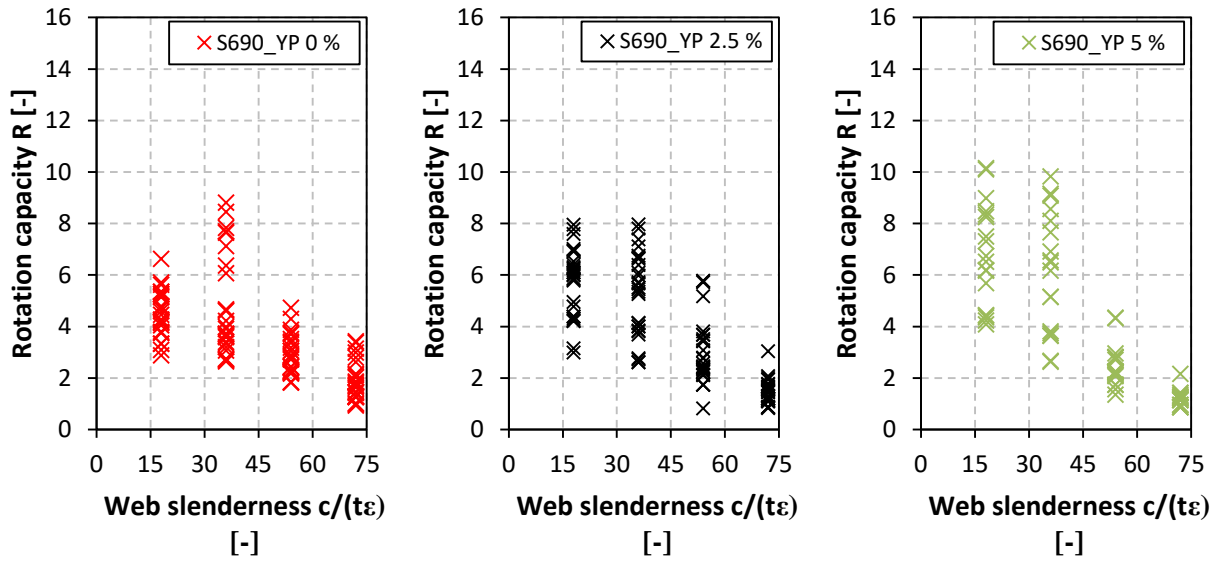


Figure 25: Influence of the three yield plateaus 0.0 % (left), 2.5 % (middle) and 5.0 % (right) versus the web slenderness on rotation capacity of S690 beams

To summarize the results, plastic design of HSS beams is generally possible, because all investigated cases reach the plastic resistance moment M_{pl} , but there have to be additional design rules, to ensure, that sufficient rotation is possible. The slenderness, especially the web slenderness has a magnificent impact on the rotation capacity. Here, additional requirements regarding new slenderness limits for plastic design of HSS are necessary. Possible options will be discussed in Deliverable D2.5. Regarding the material, a minimum yield ratio has to be present, but with the requirements of EN 1993-1-12 [9], this should be fulfilled always. The uniform elongation and the length of the yield plateau do not have a significant influence on the rotation capacity. It has to be mentioned that the combination of all three investigated material properties can lead to stronger impacts on the rotation capacities and a general statement on the “best” material properties is not possible.

Since during the presented study only widths of flanges and web heights have been varied while thicknesses remained constant (flange thickness = 12 mm and web thickness = 10 mm), certain slenderness combinations on beams made of S690 have been designed differently: The flange and web thicknesses have been changed to 10 and 8 mm, 8 and 6 mm, 15 and 10 mm, 10 and 10 mm, 15 and 12 mm, 20 and 15 mm, 25 and 20 mm, 30 and 25 mm respectively in 3 sections with different slendernesses and 3 flow curves (low, medium and high values of uniform elongation, yield ratio and strain hardening strain) resulting in 72 additional simulations. The three investigated slendernesses were:

- $c/t_{flange} = 4.50$ and $c/t_{web} = 18.00$
- $c/t_{flange} = 6.25$ and $c/t_{web} = 36.00$
- $c/t_{flange} = 9.00$ and $c/t_{web} = 72.00$

The three utilised flow curves following the definition of D1.1 are S690_LB_LB_00, S690_MW_MW_25 and S690_UB_UB_50.

The remaining parameters were equivalent to the ones of the main study. All beams had a span length of 3000 mm, stiffeners at supports and the load application with thicknesses of flange and including welds and lateral supports at six points with a width of 240 mm and stiff supports.

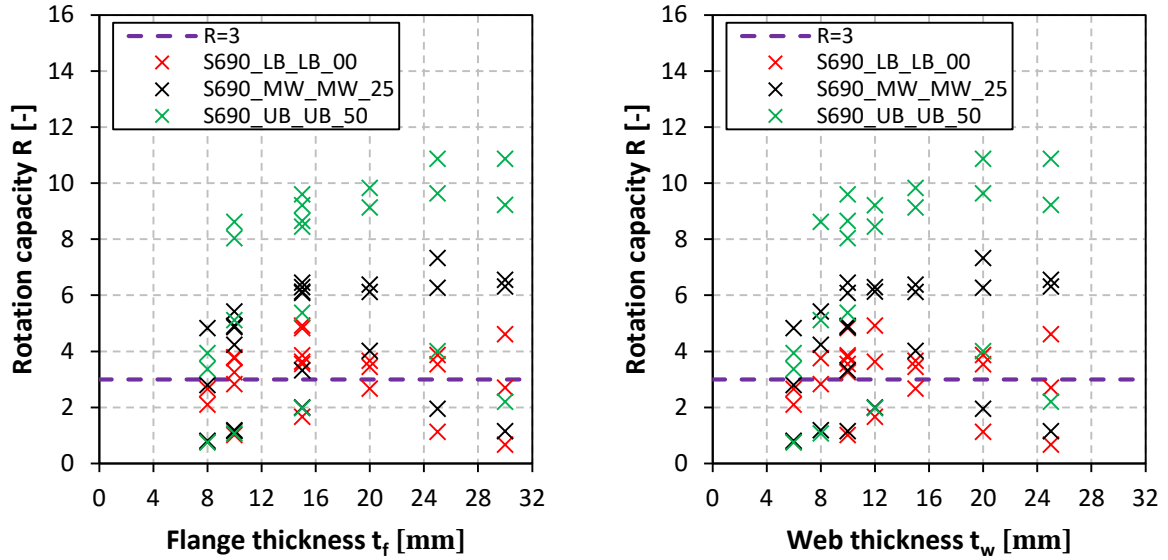


Figure 26: Rotation capacity of beams with varying flange (left) and web (right) thicknesses

The achieved rotation capacities of the beams of this additional investigation are depicted in Figure 26 versus the flange (left) and the web (right) thickness. For all three investigated flow curves (different colors) the lowest rotation capacity belongs to the beam with the slenderest cross section whereas the highest rotation capacity belongs to beam with the most compact section.

In accordance with the previous results, in general the flow curves with higher values for the yield ratio, uniform elongation and yield plateau lead to higher rotation capacities of beams with the same cross section. Thin webs ($t_w \leq 8$ mm) as well as thin flanges ($t_f \leq 10$ mm) tend to lead to low rotation capacities. But this is investigated here only combined, since the flange and web thickness were varied simultaneously.

To further investigate the influence of the thickness itself, another 42 simulations have been conducted, where the thicknesses were varied individually. Here, while the flange thickness remained constant at 12 mm, the web thickness was varied in the following steps: 6, 8, 10, 12, 15, 20, and 25 mm. Additionally, the web thickness was held constant at 10 mm, while the flange thickness was varied in the following steps: 8, 10, 12, 15, 20, 25 and 30 mm. Again, the three slenderness levels have been used and only one flow curve (the average S690_MW_MW_25) was investigated.

Figure 27 presents the evaluation of these investigations.

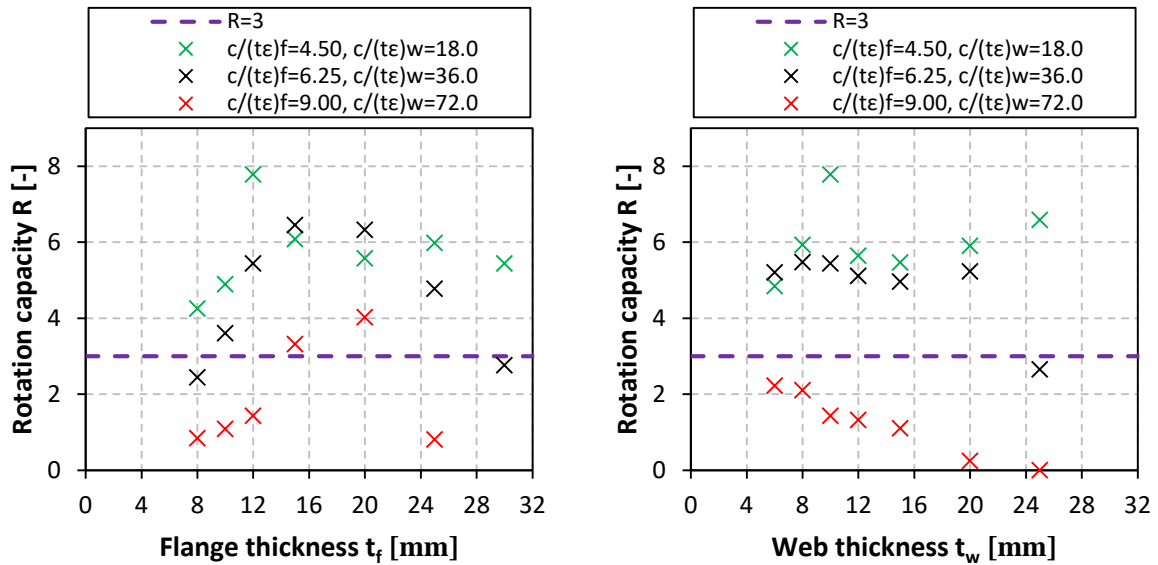


Figure 27: Results of the additional study varying flange and web thickness individually

Extreme combinations for web and flange thicknesses (e.g. $t_f = 30$ mm and $t_w = 10$ mm or $t_f = 12$ mm and $t_w = 25$ mm) lead to beams with low rotation capacities. These combinations however, seem to be not realistic.

In addition to this, the influence of “hybrid homogeneous beams” has been exemplarily explored. These beams are in general homogenous, thus made of the same steel grade, but have different flow curves for this steel grade in the flanges and the web. The utilized flow curves for a steel grade of S690 in the flange and the web are listed in Table 2. Each combination is identified by an index.

The remaining parameters were held constant. The same loading condition with an average cross section has been used, which had a web slenderness of 36ϵ and a flange slenderness of 6.25ϵ .

Table 2: Used flow curves in the “hybrid homogeneous beams” for the steel grade S690 and their indices

Index	Flow curve flange	Flow curve web
1	MW_MW_25	MW_MW_25
2	LB_LB_00	UB_UB_50
3	UB_UB_50	LB_LB_00
4	UB_UB_50	UB_UB_50
5	LB_LB_00	LB_LB_00
6	MW_MW_25	UB_MW_25
7	MW_MW_25	LB_MW_25
8	UB_MW_25	MW_MW_25
9	LB_MW_25	MW_MW_25

Figure 28 depicts the results for the rotation capacity of the “hybrid homogeneous beams” as a function of the indices from Table 2. The existing rotation capacities vary from 6.45 to 11.50. This is caused only by “different materials”, so different properties of the flow curve for the same steel grade, and shows again the huge impact of the flow curve. Combination no. 4 shows the highest rotation capacity and has also the “best” flow curves with the highest yield ratio, highest uniform elongation and a long Lüder’s (yield) plateau. The worst result is given by the combination no. 5, which has the “worst” flow curve properties (lowest yield ratio, lowest uniform elongation and no Lüder’s plateau). In combinations no. 6 and 7, the yield ratio of the web is changed to high and low. The result is that the lower yield ratio in the web (combination no. 7) leads to in total lower rotation capacity compared to combination no. 1 with the average flow curves (from 11.31 to 10.70). Compared to combination no. 6 which has the higher yield ratio in the web, the rotation capacity is unexpectedly a bit higher (10.70 to 8.12). The comparison of combinations 8 and 9 do the same thing for the flange. Here, the yield ratio of the flange material is set to high (combination no. 8) and low (combination no. 9). The higher yield ratio in the flange leads to a better rotation capacity than the lower yield ratio in the flange. But as well as before, in total the rotation capacity goes down for combination no. 8 (from 11.31 to 10.61).

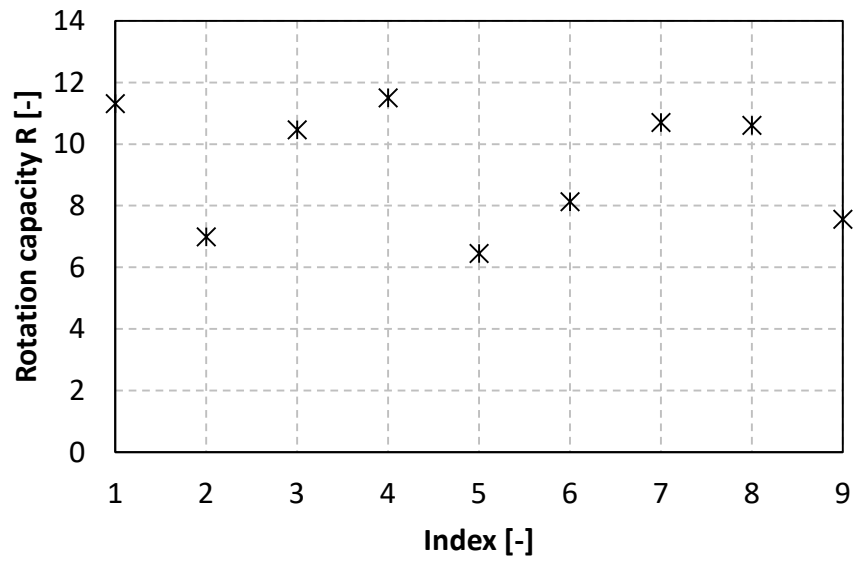


Figure 28: Rotation capacities of “hybrid homogenous beams”

These investigations show again that the yield stress ratio, uniform elongation and yield plateau each have a significant influence on the rotation capacity. Final recommendations on optimized material properties needs further study.

3.2 Rotation capacity depending on hybrid sections, length, boundary conditions and loading

During this additional study, the main influencing characteristics, such as slenderness and material characteristics are mainly held constant, while the remaining parameters have been assessed. The following sections describe the main results of the study.

3.2.1 Buckle eigenform

Before discussing the influence of the imperfection size, it has been found, that also the buckle eigenform has a large influence on the results in terms of rotation capacity. The buckle eigenform defines the shape of imperfection, which depicts the worst case scenario. In practice, imperfection shapes can be absolutely random.

The results show that three different types of buckle eigenforms play a role without any specific order (Figure 29). The first form is point symmetrical to the mid-span and buckles on both sides of the stiffener (as observed in the experimental tests). The second form is symmetric with respect to the mid-span, whereas the third one only shows buckling on one side of the stiffener.

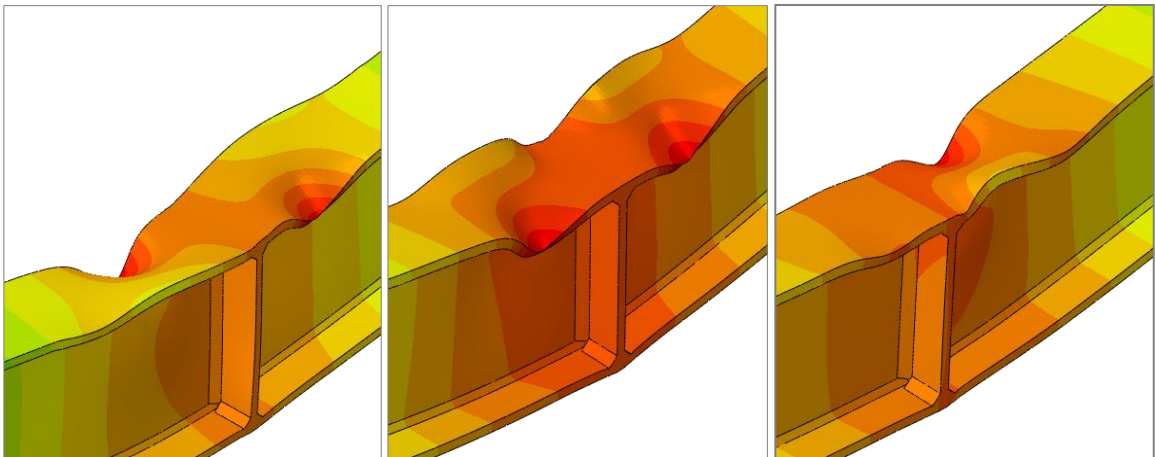


Figure 29: Three types of buckle eigenform: point symmetrical (left), axially symmetric (middle) and one-sided buckling (right)

These three buckle eigenforms have an influence on the slope of the moment-rotation curve and consequently on the rotation capacity. Only eigenforms with a positive buckle eigenvalue are considered in the analysis. Therefore, Figure 30 and Figure 31 show only the results for buckling in the upper flange. Beams with point symmetrical buckle eigenforms have a minor rotation capacity than those with axially symmetric forms and the slope of the curve is steeper after reaching the highest point of the curve. If the buckling is only on one side of the stiffener, the rotation capacity is slightly higher than for the point symmetrical form and the curve shows a higher maximum.

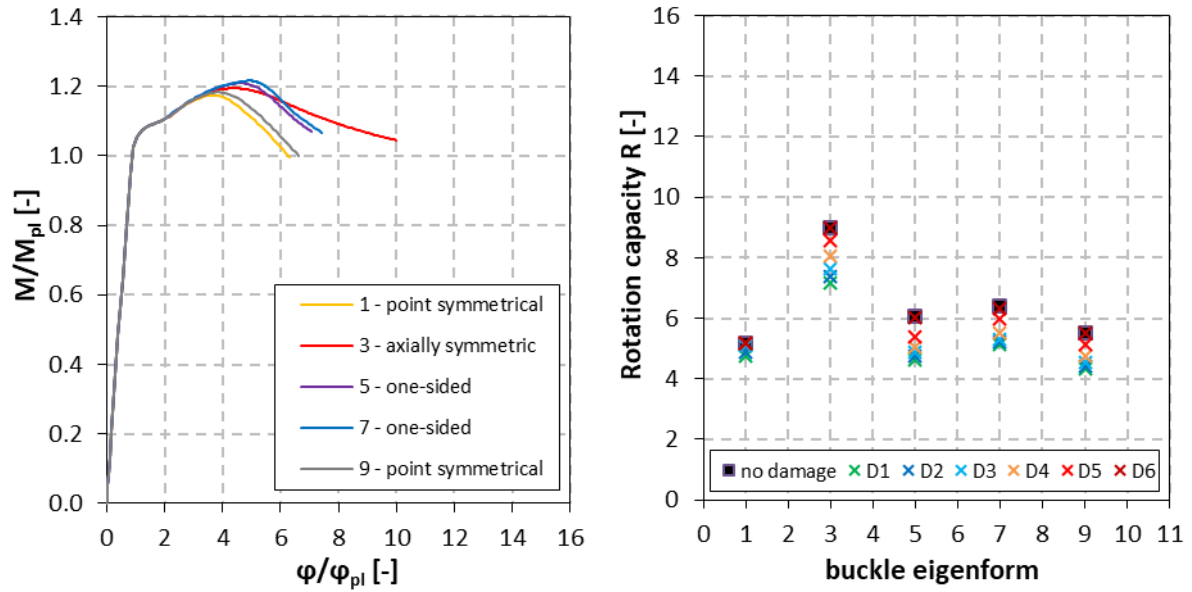


Figure 30: Influence of the buckle eigenform on the moment-rotation curve (left) and rotation capacity (right) of 075_050_S690

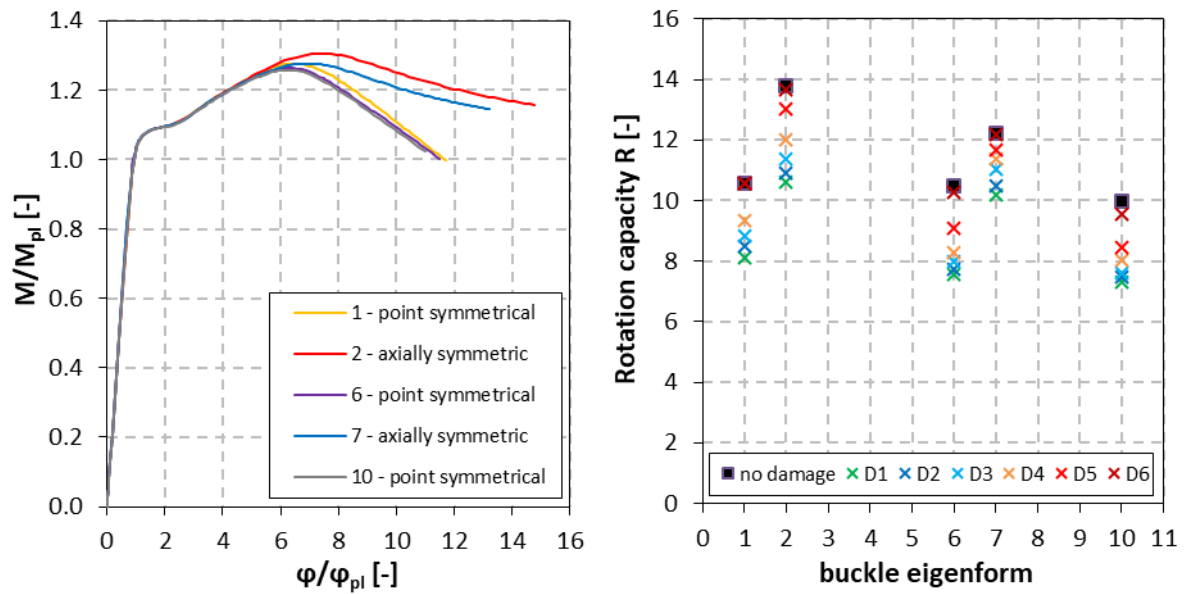


Figure 31: Influence of the buckle eigenform on the moment-rotation curve (left) and rotation capacity (right) of 075_050_S500

Compact beams show the same behaviour, but the influence is minor and the buckle deformation is hard to identify. On the other hand, the slender cross-sections are strongly influenced by buckling and show also different results for the various eigenforms.

3.2.2 Imperfection size

In this section, the influence of the size of the imperfection on the rotation behaviour is presented. First, the relevant buckle eigenform is implemented in the load bearing analysis with five different sizes of imperfections ranging from 0.5 mm to 10 mm:

- 0.5 mm
- 1 mm
- 2.5 mm
- 5 mm
- 10 mm

Figure 32 shows the results for the 075_050_S690 beams with rigid lateral supports and for the ones with lateral supports in the form of springs. In the right diagram of Figure 32, the lower point always corresponds to the simulations with springs and the upper point always refers to the simulations with rigid supports. The trend for the moment-rotation curves is almost identical for both the rigid and spring supports, only that the values of the spring supported beam are slightly smaller. Both show that with a greater size of imperfection, the rotation capacity is decreasing.

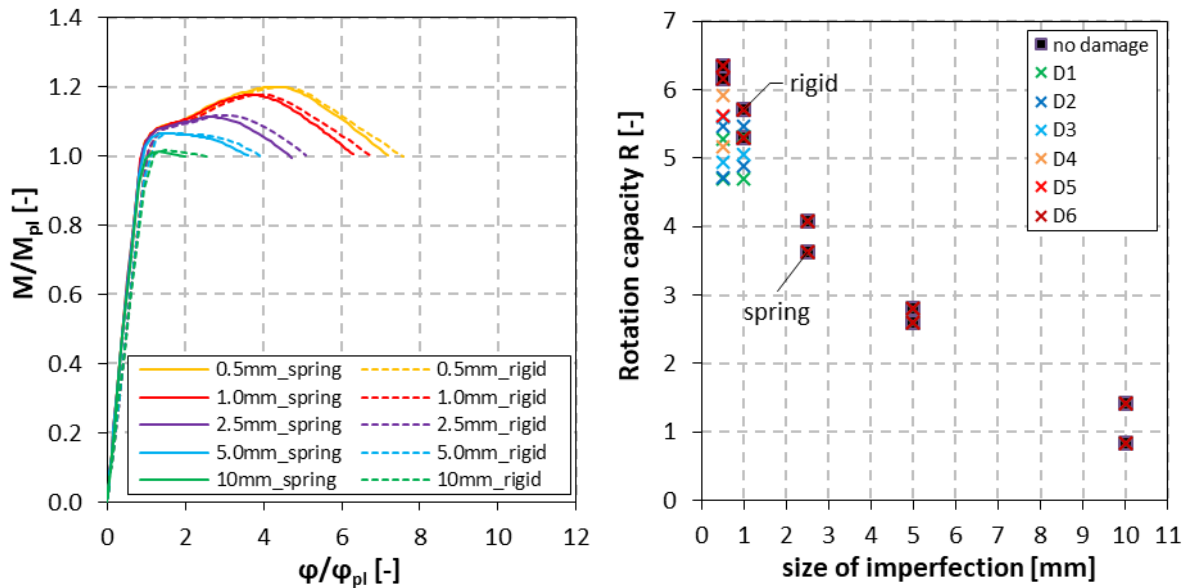


Figure 32: Influence of the size of imperfection on the moment-rotation curve (left) and rotation capacity (right) of 075_050_S690

However, the compact beams show less of an impact from the increasing size of imperfection than the other cross-sections, especially beams with a steel grade of S500 (Figure 33). The moment-rotation curves show that the maximum moments of the different beams decrease and all beams fail due to the occurrence of cracks. Therefore, the rotation capacity remains the same level or is even slightly higher. Beams with a steel grade of S690 show a steeper descending branch of the moment-rotation curve. In the left diagram of Figure 33, the upper points always refer to the results of beams with the steel grade of S500, while lower points always refer to those of S690.

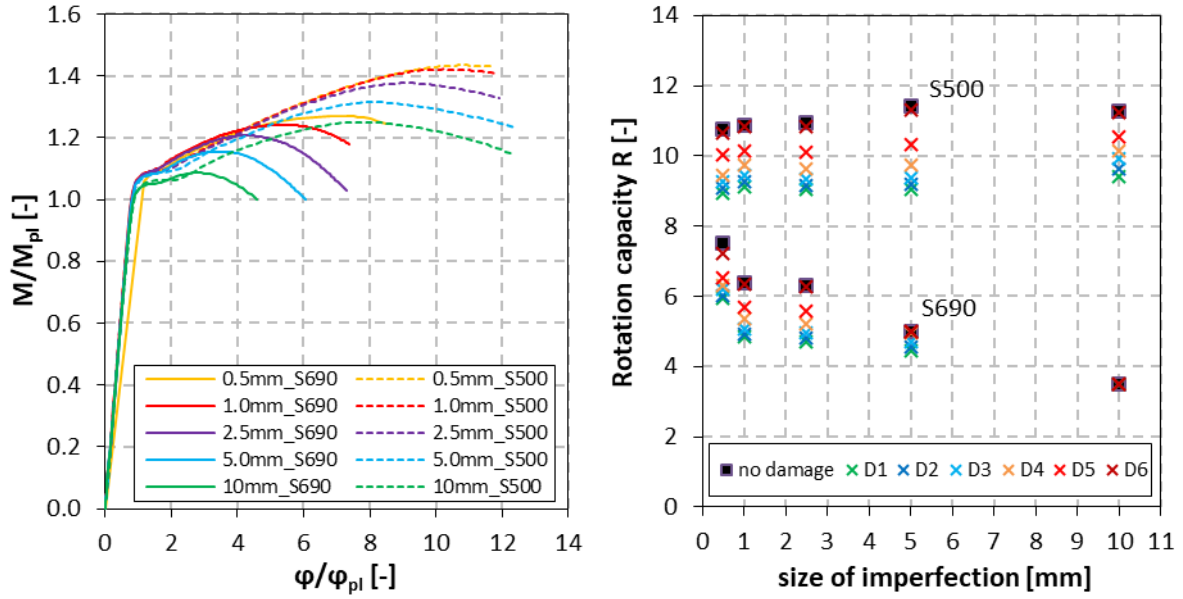


Figure 33: Influence of the size of imperfection on the moment-rotation curve (left) and rotation capacity (right) of 050_025_S690 and 050_025_S500

3.2.3 Beam length

In this study of the beam length, the reference beams are modelled in seven different lengths, varying from 1000 mm to 10000 mm. In order to consider the different beam lengths regarding the rigid lateral supports, the width of the lateral support lengthens likewise to the span length. Therefore, the distance from the lateral support to the load application point is increasing as well.

Only beams with short lengths ranging from 1000 mm to 2000 mm are influenced by the moment-shear-force-interaction. The two most slender beams with the length of 1000 mm (1000_100_S690 and 1000_100_100_S500) do not have a sufficient load capacity because the shear force exceeds their resistance. Hence, only 40 beams can be used for the first part of the length study.

In case of both investigated steel grades, the rotation capacity is decreasing simultaneously with an increasing beam length, Figure 34. The curves of the medium slender beams show almost a linear decrease in the rotation capacity until the length of 4000 mm for the beams with the steel grade of S690 and 6000 mm for beams of S500.

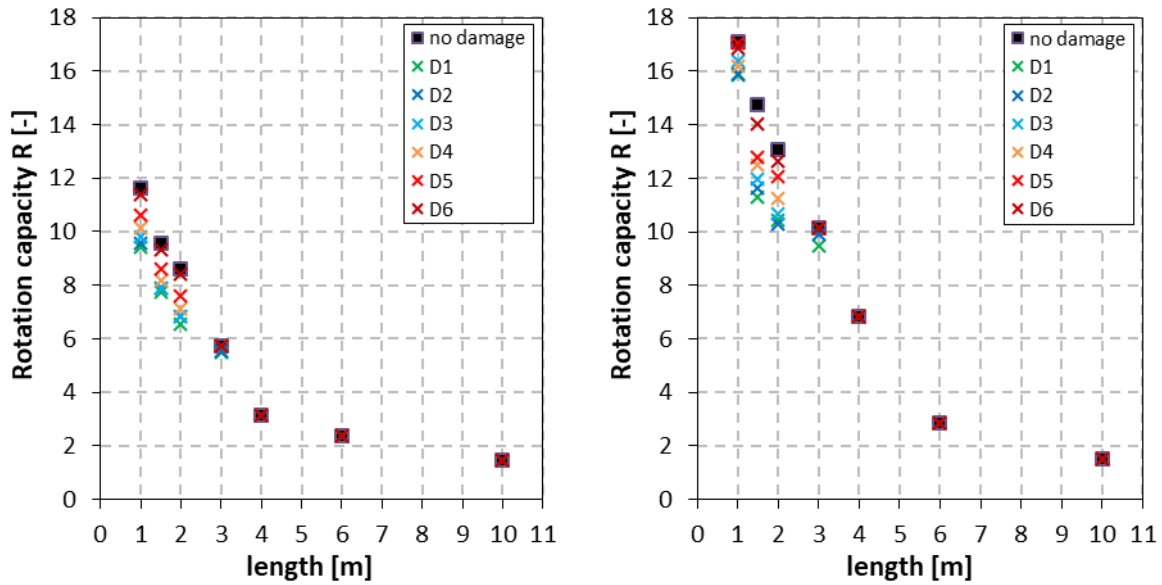


Figure 34: Influence of the beam length on the rotation capacity of 075_050_S690 (left) and 075_050_S500 (right)

Figure 35 shows that the slenderness of the beam strongly influences the rotation capacity. It is higher for compact beams in comparison to slender cross-sections. Evidently, slender beams are more influenced by buckling.

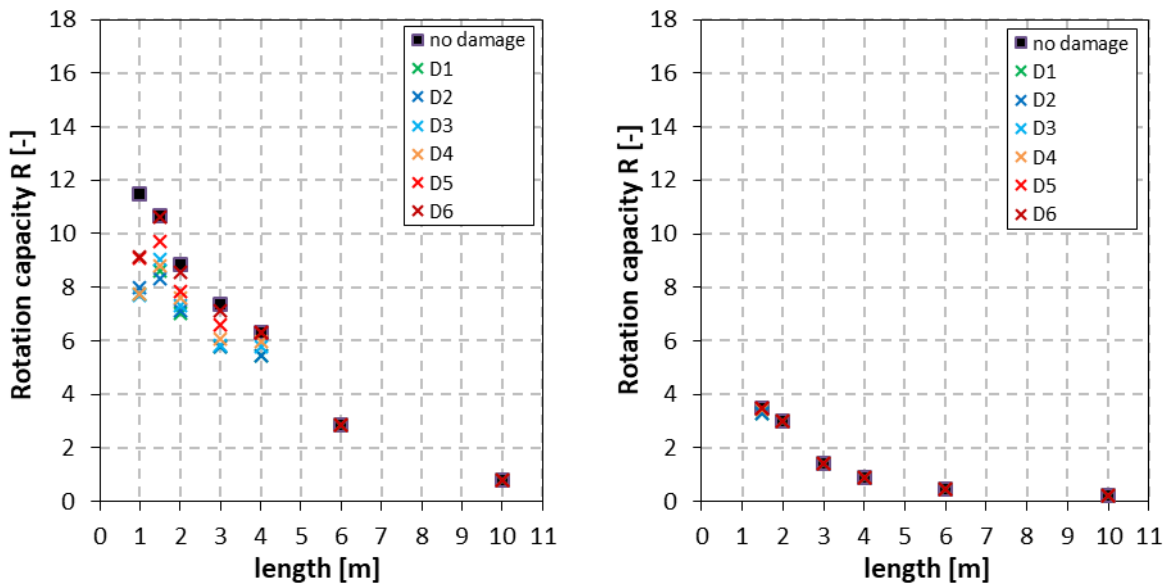


Figure 35: Influence of the beam length on the rotation capacity of 050_025_S690 (left) and 100_100_S690 (right)

The plastic rotation shows a different behaviour than the rotation capacity (Figure 36). First, the plastic rotation increases until it reaches a certain length and then decreases in form of a parabola.

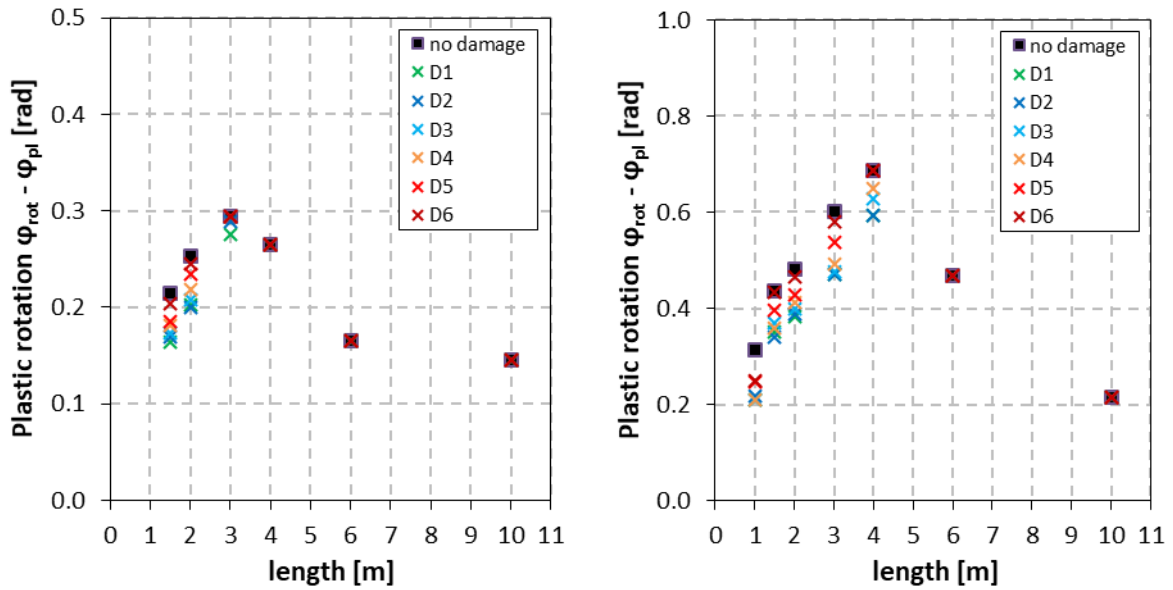


Figure 36: Influence of the beam length on the plastic rotation of 075_050_S500 (left) and 050_025_S690 (right)

Moreover, the shorter beams show a failure due to the occurrence of cracks, whereas the longer beams fail because of buckling, as also observed in the experimental investigations. In Figure 37, the curves of the longer beams decrease due to buckling, whilst the curves of the three shorter beams show crack initiation before the curves interact a second time with the M_{pl} -level ($M/M_{pl} = 1.0$). This behaviour can be influenced by the positioning of the lateral supports. Therefore, the second part of this length study investigates this influence on the rotation capacity in detail.

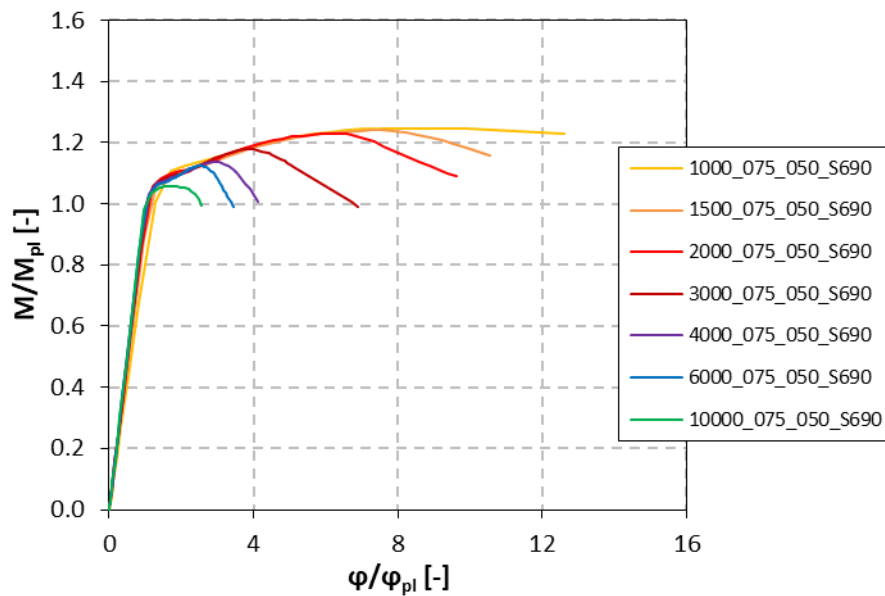


Figure 37: Influence of the beam length on the moment-rotation curves of 075_050_S690

In the first part of the length study, the four lateral supports are located at every sixth of the beam length, except for the supports and the load application point. For this reason, the distance from the lateral support to the load application is very large for the longer beams. The second part investigates the influence of the position of the lateral support. This time, the lateral supports closer to the mid-span are placed at the same distance of 200 mm to the load application and are therefore located closer to the load introduction point.

Figure 38 shows the difference in the rotation capacity for the first and second part of the length study. The observed trend of a decreasing rotation capacity with an increasing beam length is almost identical. However, the rotation capacity of the longer beams is slightly less in the first length study.

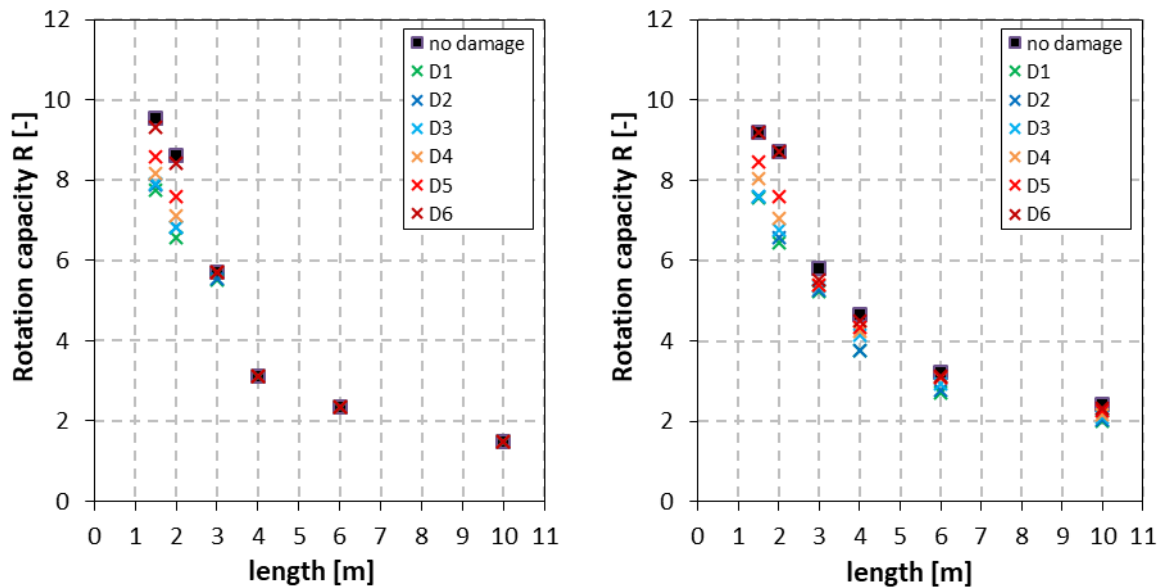


Figure 38: Rotation capacity of the first (left) and the second part of the length study (right) of 075_050_S690

3.2.4 Stiffness of lateral support

In practice, lateral supports are not always rigid, e.g. in the form of a secondary supporting structure of steel purlins. Consequently, the support can be simulated by using springs considering a certain stiffness of the lateral support. The lateral supports in this study have nine different spring stiffness values ranging from 0 N/mm up to $5 \cdot 10^9$ N/mm to investigate their influence on the rotation capacity:

1. 0 N/mm
2. $5 \cdot 10^1$ N/mm
3. $5 \cdot 10^2$ N/mm
4. $5 \cdot 10^3$ N/mm
5. $5 \cdot 10^4$ N/mm
6. $5 \cdot 10^5$ N/mm
7. $5 \cdot 10^6$ N/mm

8. $5 \cdot 10^7$ N/mm
9. $5 \cdot 10^9$ N/mm

The results show that the beam is strongly weakened due to local buckling, unless a certain lower spring stiffness is reached and the upper flange deforms in a global S-shape. Therefore, the rotation capacity is increasing with higher spring stiffness values, since the global buckling influence decreases (Figure 39). When the lateral support exhibits a certain spring stiffness, the rotation capacity maintains a certain level, though with some exceptions, depending on the buckle eigenvalue implemented in the load bearing analysis.

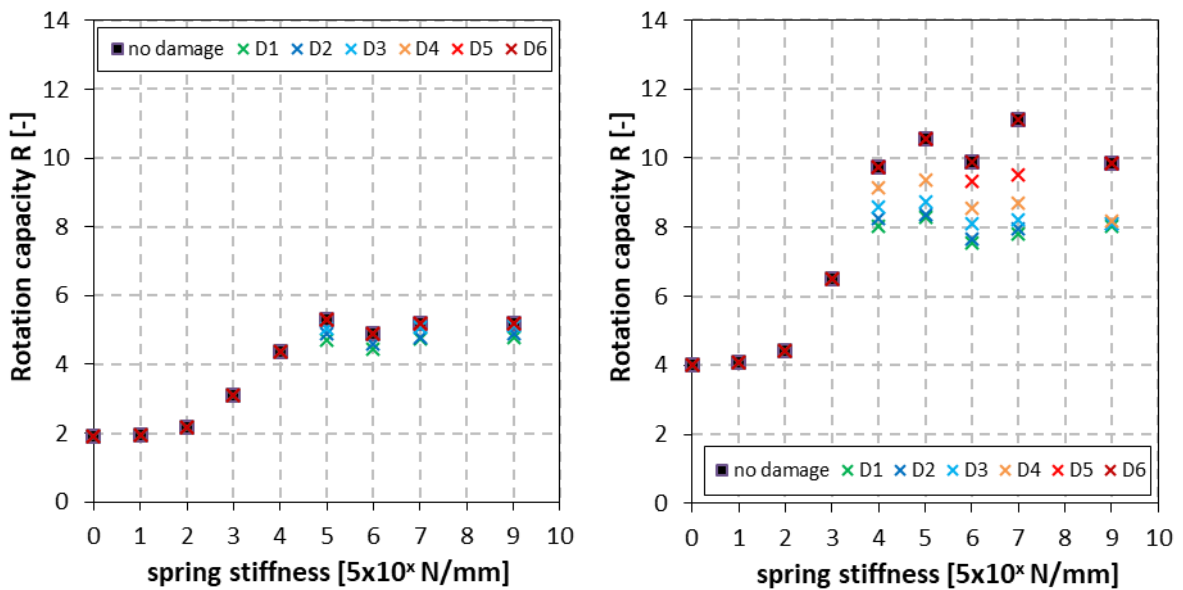


Figure 39: Influence of the spring stiffness on the rotation capacity of 075_050_S690 (left) and 075_050_S500 (right)

The decisive imperfection shapes derived from the buckle analyses have different shapes, which are influenced by the spring stiffness of the lateral support (Figure 40) and further on influence the simulation results of the load bearing analysis.

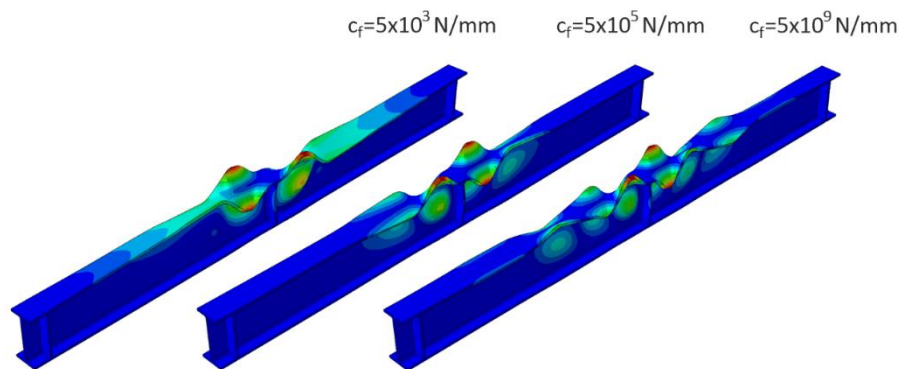


Figure 40: Decisive buckle eigenforms from buckle analysis with different spring stiffness values (with scale factor of 100)

3.2.5 Application of stiffeners

Part 1-1 of the Eurocode 3 [8] demands for stiffeners to be installed where loads are applied. In the stiffener study, all six reference beams are modelled without stiffeners to investigate their influence on the behaviour of the beam.

The results show that, among other criteria, the influence of the stiffeners depends on the cross-section. Slender beams with a high use of the CSC 1 (100_100) do not show adequate moment rotation behaviour. Due to premature buckling, the internal moment does not reach the plastic moment resistance M_{pl} . In contrast, stiffeners appear to have almost no influence on compact beams, apart from the fact that the rotation capacity is even higher for the 050_025_S500 beam without stiffeners, Figure 41. The beam with stiffeners fails due to cracking announced by the damage criterion before reaching the M_{pl} -level the second time, whilst the beam with stiffeners fails later due to local buckling. The state of stress in the moment maximum is changed due to the application of the stiffeners, leading to a different damage behaviour.

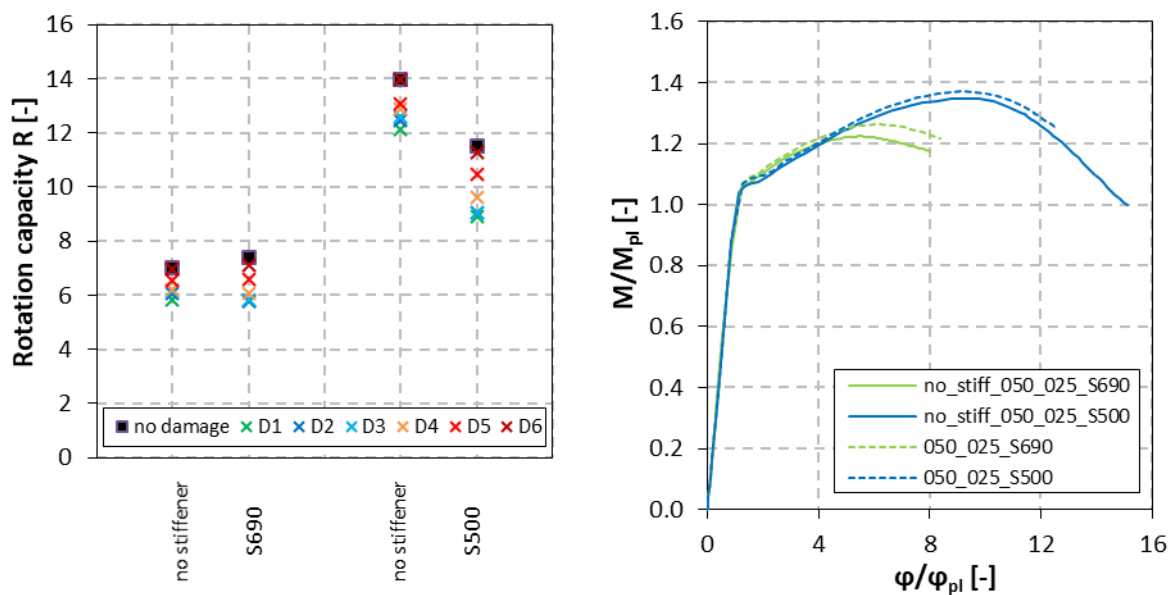


Figure 41: Influence of the stiffener on the rotation capacity (left) and on the moment-rotation curve (right) of 050_025_S500 and 050_025_S690

The results for the beams with a medium slenderness show a different behaviour for the rotation capacity (Figure 42). Their rotation capacity is smaller compared to the beams with stiffeners. Stiffeners can induce a coupling effect of the upper and lower flange which then increases the M/M_{pl} -ratio especially after the first buckling effects occur. Figure 42 also shows that the curves of the beam with steel grades of S500 and S690 without stiffeners are almost identical. The steel grade of the beam has therefore no influence on its behaviour because the plastic material behaviour cannot be exploited in the short section between the intersections of the curve with the M_{pl} -level.

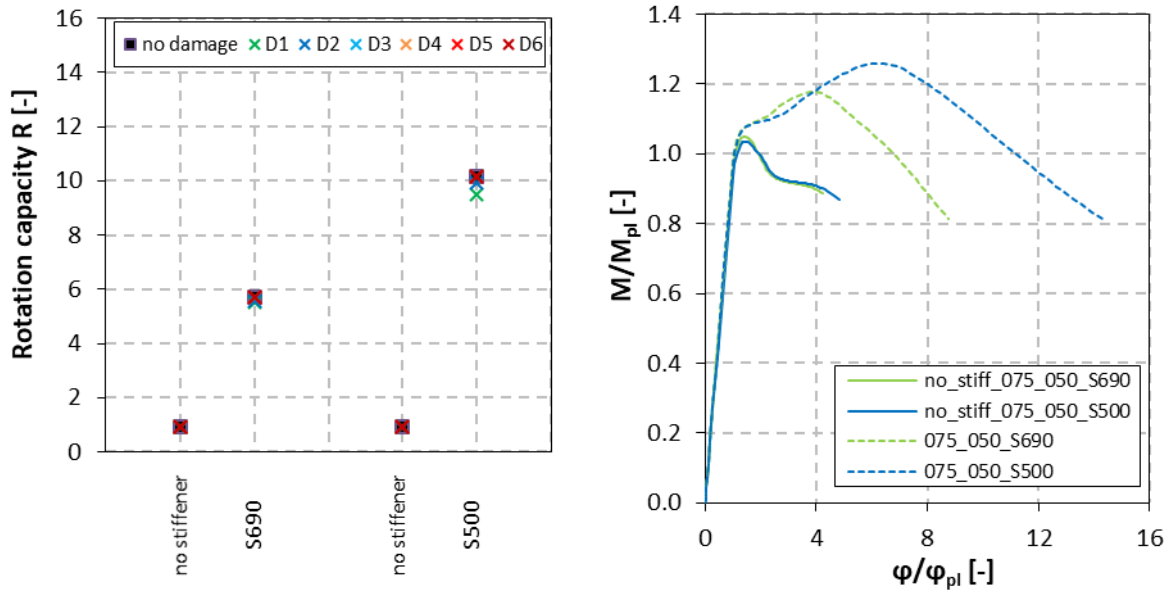


Figure 42: Influence of the application of stiffeners on the rotation capacity (left) and on the moment-rotation curve (right) of 075_050_S500 and 075_050_S690

3.2.6 Hybrid beams

In this study, the hybrid beams are designed with steel grade S690 for the flanges and steel grades of S355 and S500 for the web. Beams with S500 for the flange and S355 for the web are investigated as well. Figure 43 exemplarily shows several hybrid cross sections.

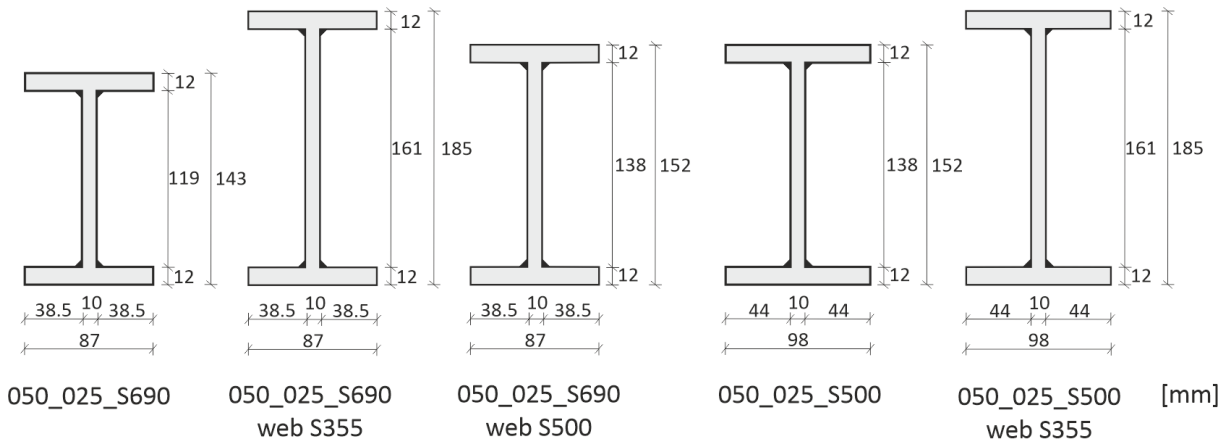


Figure 43: Compact cross-sections (050_025) of the hybrid beams compared with the homogeneous beams

The moment-rotation curves of the hybrids are always located between the curves of the homogeneous beams with that same material in their flange and web. For example, the curve of the hybrid beam S690-S500 is located between the curve of the homogeneous beams with the steel grade of S690 and S500 (Figure 44). Though, the rotation capacity is always slightly higher than the results of the homogeneous beams.

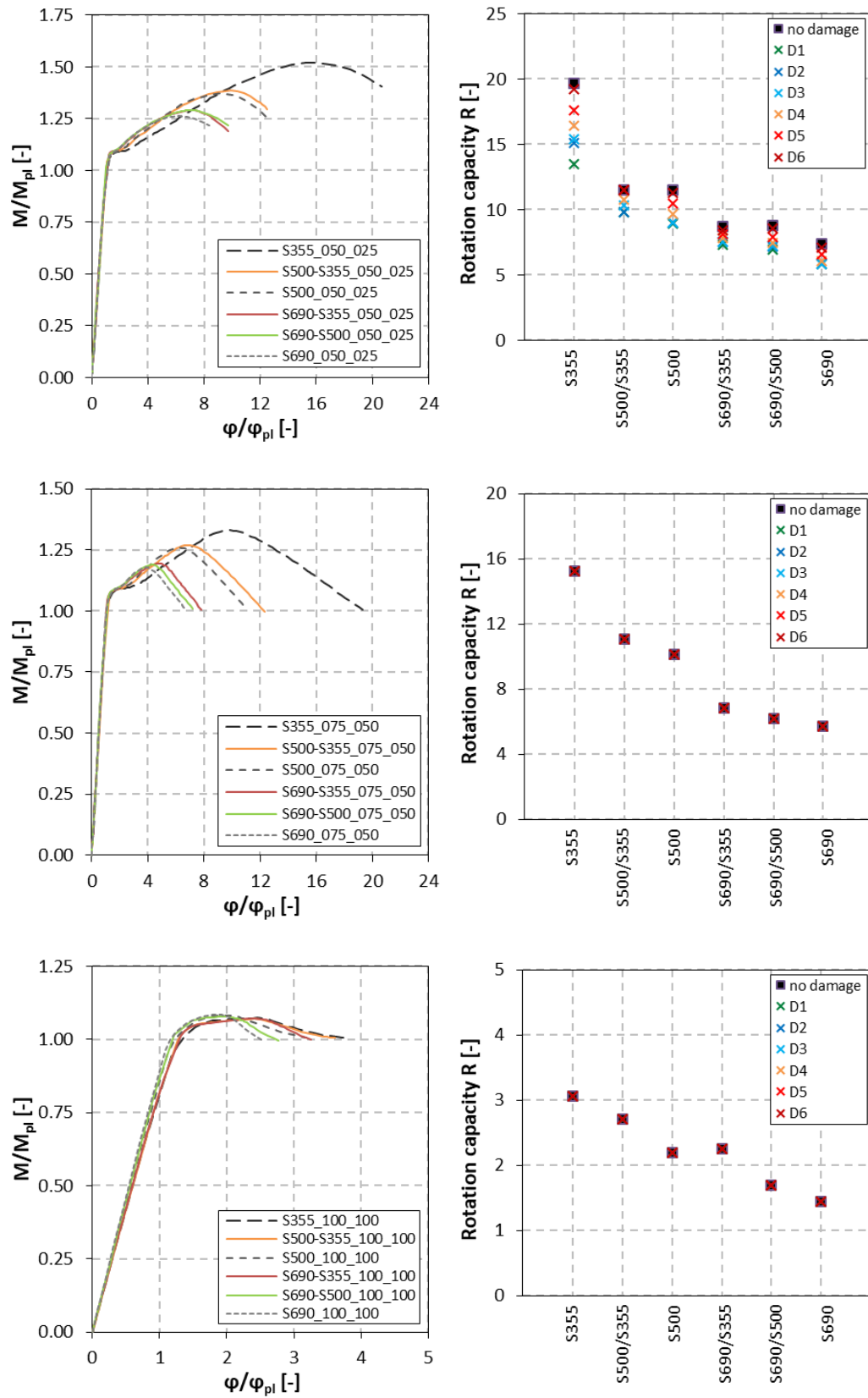


Figure 44: Influence of web steel grade on moment-rotation curve and rotation capacity of 050_025 (upper charts), 075_050 (middle charts) and 100_100 (lower charts)

The moment-rotation curves for beams of the same slenderness (050_025, 075_050 or 100_100) show the same shape, only the highest moment M_u is different within the same slenderness for the different beams. The form of the beam deformation confirms this observation. Figure 45 shows the deformations of the medium slender hybrid beams.

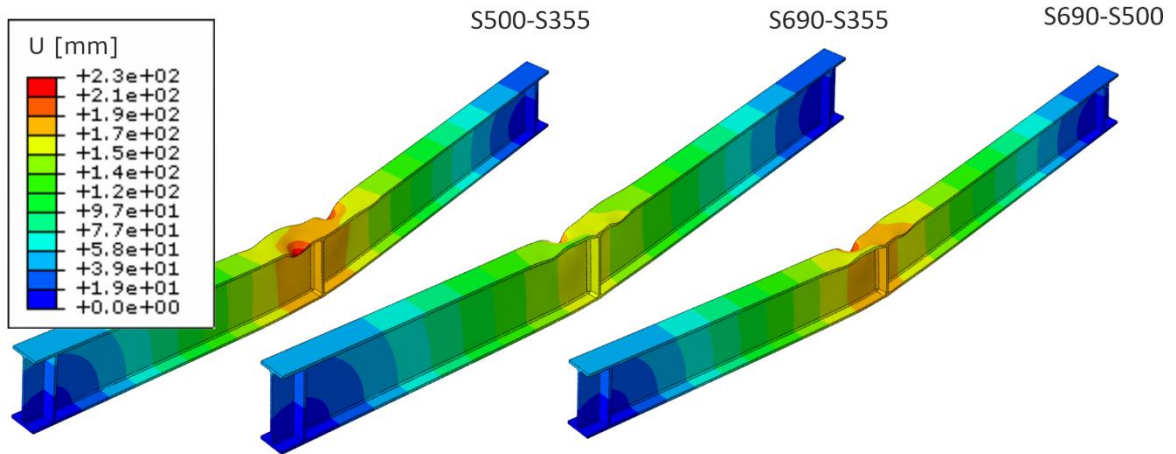


Figure 45: Deformation figures at failure of the hybrid beams with slenderness 075_050

Figure 46 shows the improvement of the rotation capacity of hybrid beams in comparison to homogeneous beams with the same steel grade as the one of the flanges from the hybrids. With an increase in the cross-section slenderness, the rotation capacity of the hybrid beams improves compared to the homogeneous beams, although at the same time, the absolute rotation capacity decreases. Hence, even with this improvement, not all slender hybrid beams might be able to reach a sufficient capacity for plastic design.

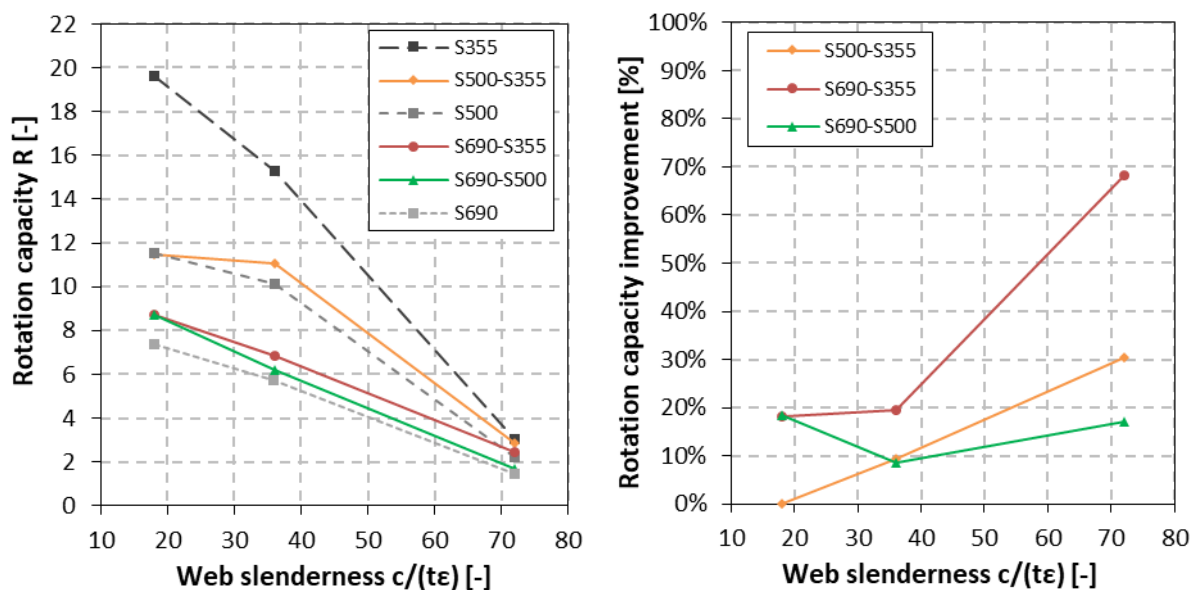


Figure 46: Influence of web steel grade on the rotation capacity regarding the web slenderness

The rotation capacity of the hybrid beams is always the same or improved compared to the homogenous beams. Since hybrids are cost efficient, the hybrid beams have advantages compared to homogeneous beams if the load capacity is ensured as well. It has to be kept in mind that a potential improvement of rotation behaviour due to a hybrid section always leads to a reduction of load bearing capacity.

3.2.7 Loading condition

Alongside the length, the steel grades and the lateral support, the load situation is a strong influence on the rotation capacity as well. Normally, the three-point-bending test (3point) is the common test used to investigate the rotation capacity. In this study, it is replaced by differing loading conditions. The beams are modelled with two different four-point-bending tests (4point_far and 4point_near), as well as beams with a uniformly distributed load (udload). Figure 47 gives an overview of the three additional loading situations that are being investigated. The lateral supports have the same position and length in every model, independent of their load situation. Stiffeners are always added at the load application point, and for the beams with a uniformly distributed load, the stiffeners are placed in the centre of the span.

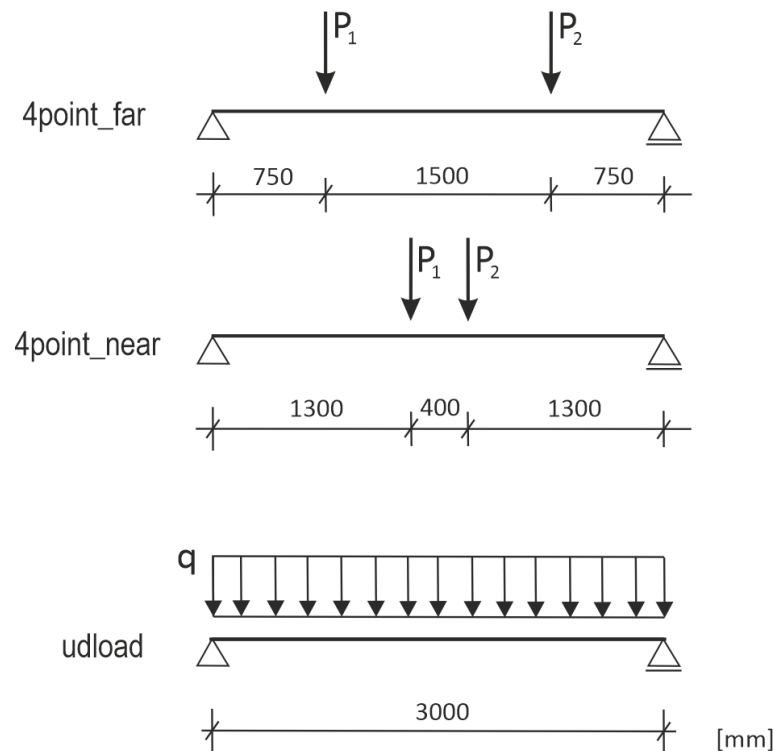


Figure 47: Four-point-bending test (4point_far and 4point_near) and uniformly distributed load (udload)

The elastic rotation ϕ_{pl} has to be adjusted for each loading and also, the calculation of the moments must be modified, as well as the moment-shear-force-interaction according to the load situation.

Four-point-bending test

Figure 48 shows the moment-rotation curves of the four-point-bending tests with loads far distanced from each other and with a steel grade of S500. The curves of the compact and medium slender beam are almost identical and their plastic branches are near and parallel to the M_{pl} -level. The slender beam fails due to buckling and possesses a smaller rotation capacity in comparison to the other cross-sections. The beam 4point_far_100_100_S500 is influenced by the moment-shear-force-interaction which reduces the plastic moment resistance and therefore, its values of the normalized moment-rotation curve are higher.

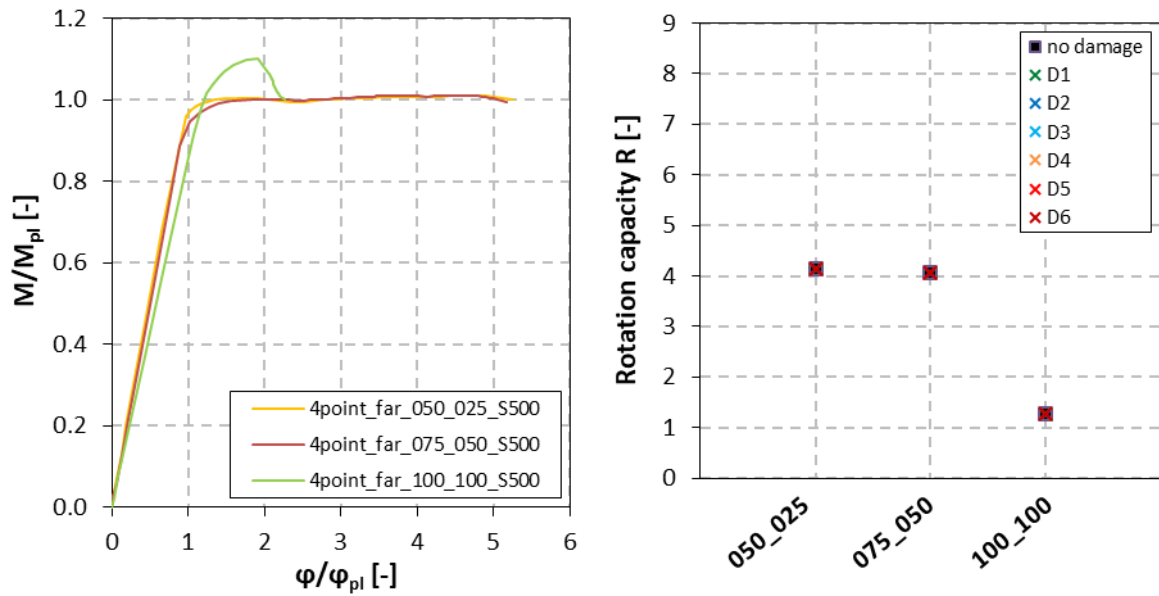


Figure 48: Moment-rotation (left) curve and rotation capacity (right) of 4point_far_S500

In contrast to the S500 beam, the compact beam of S690 has a strain hardening section and therefore a higher rotation capacity (Figure 49). The medium slender beam is close and parallel to the M_{pl} -level, just like the beam of S500, but does not reach M_{pl} . Hence, the beam has no rotation capacity at all. The slender beam fails because of local buckling and has a smaller rotation capacity, similar to the slender beam of S500.

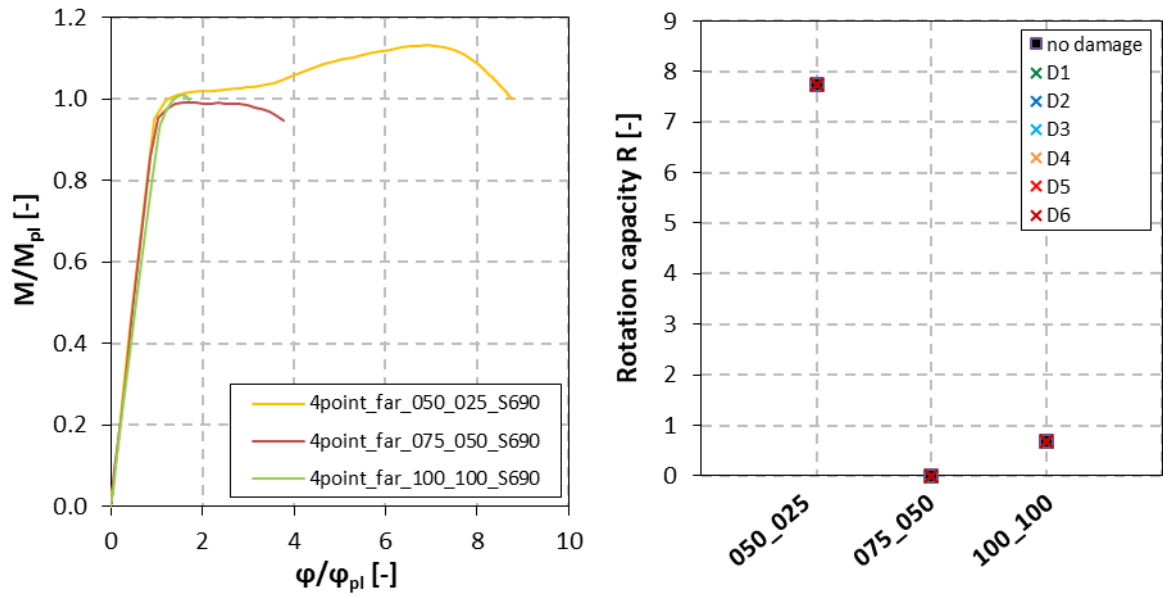


Figure 49: Moment-rotation curve (left) and rotation capacity (right) of 4point_far_S690

The left graph in Figure 50 shows the moment-rotation curves of the four-point-bending tests, with loads close to one another, whilst the graph on the right side pictures the results of the three-point-bending tests. The behaviour of the moment-rotation curves of these four-point-bending tests shows more similarities to the three-point-bending tests than to the other four-point-bending tests, where the distance between the loads is relatively large. Nevertheless, the curves are closer to the M_{pl} -level.

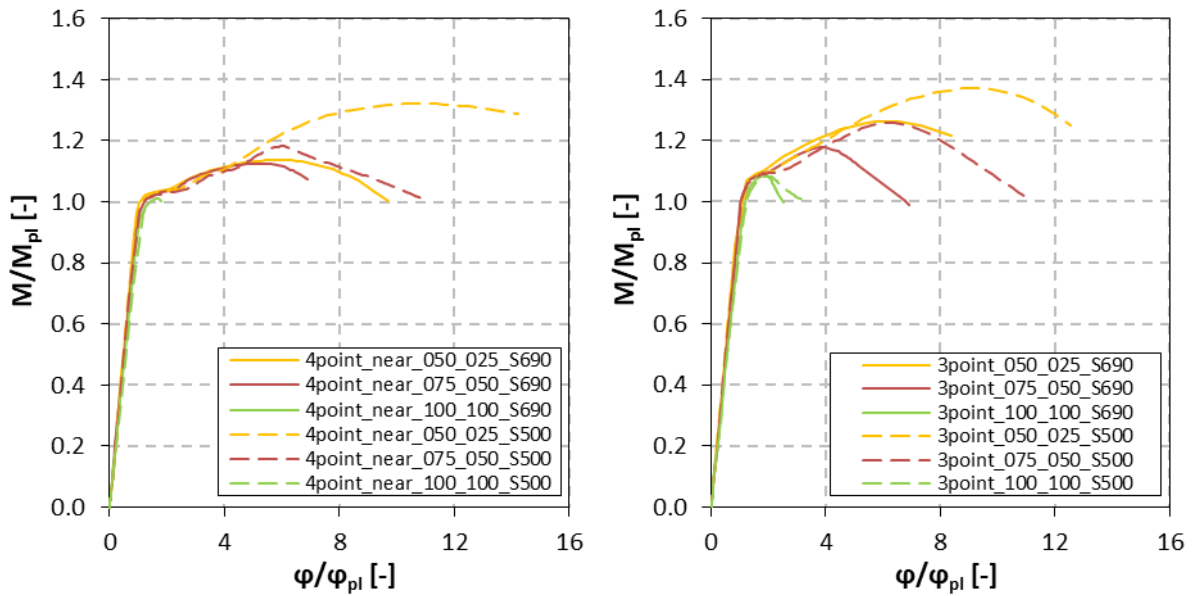


Figure 50: Moment-rotation curve of 4point_near (left) and 3point (right)

Comparing the rotation capacity of these two tests, the results seem to be influenced by the cross-section. The rotation capacity of the compact beams is higher in the four-point-bending test, while

the capacity is higher in the three-point-bending test for the slender beams. Only the medium slender cross-section shows almost the same results for both tests. In Figure 51, the upper points always refer to the results of beams with the steel grade of S500, while lower points always refer to those of S690.

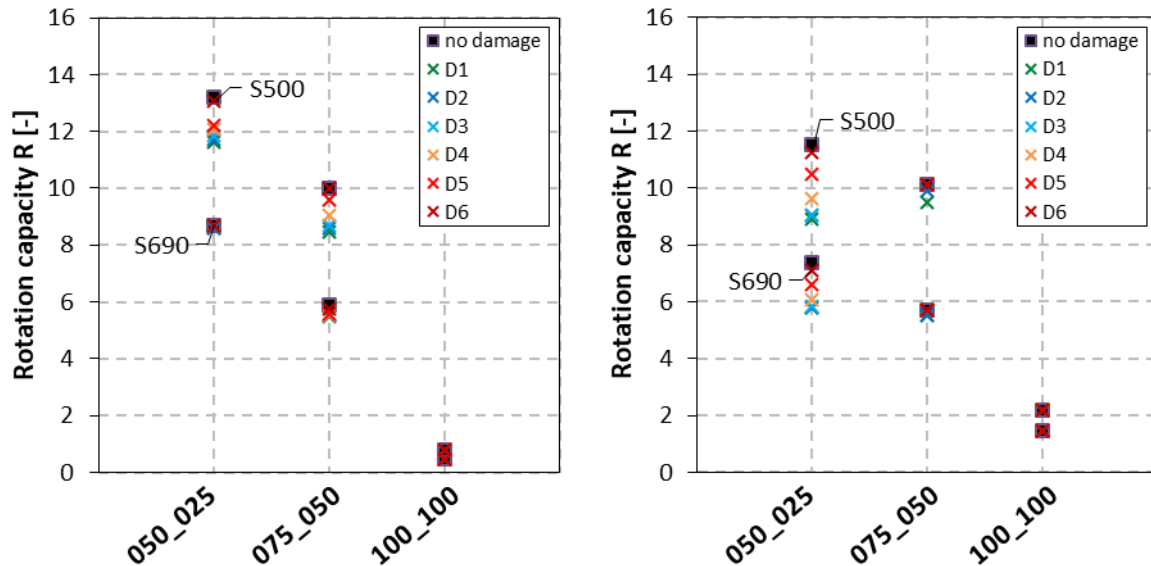


Figure 51: Rotation capacity of 4point_near (left) and 3point (right)

Uniformly distributed load

The load for the beams under a uniformly distributed load is applied as a steady pressure on the complete upper surface.

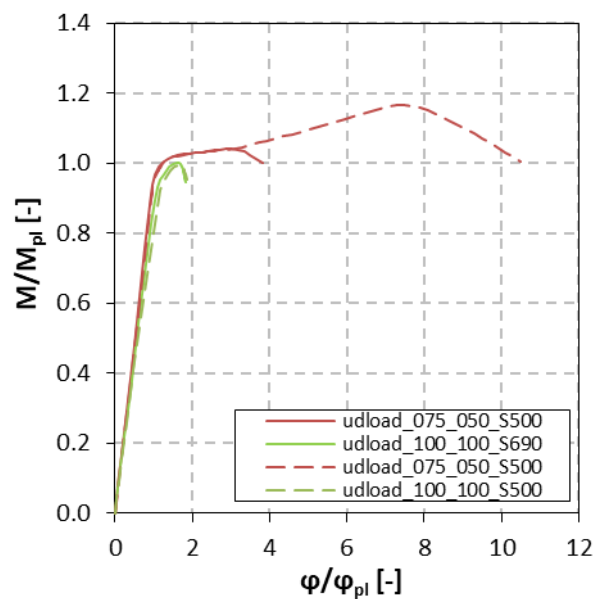


Figure 52: Moment-rotation curve of udlload

Figure 52 shows the moment-rotation curve of the beams with medium slender and slender cross-sections. The slender beams show almost no rotation capacity because the beam of S690 does not reach M_{pl} and the curve of S500 intersects with the M_{pl} -level, only to then decrease again. Beam 075_050_S500 shows strain hardening in a relatively large area and therefore a high M_u/M_{pl} -value, leading to a high rotation capacity compared to the beam of S690.

The results of the various loading conditions lead to no well-defined conclusion. Different cross-sections and steel grades show different behaviours. In general, it can be stated that load conditions with concentrated load introduction (3-point bending, close loads in four-point bending) show higher M_u/M_{pl} ratios and smaller rotation capacities. For more equally distributed loads (uniform load, more distanced four-point bending) the M_u/M_{pl} ratio is lower, in some cases even M_{pl} isn't reached, while the rotations are higher.

Also, the lateral support might have an influence on the results because different loading situations could demand for another bracing of the beam. Stiffeners might also influence the bending and rotation behaviour, as already analysed in chapter.

4 SUMMARY

In the following, results of work package 2.3 “Numerical simulation program on beams” are summarized.

First, in chapter 2.1, a numerical model for the simulation of I-girders under moment-rotation loading situations developed with the FE-program ABAQUS 6.14 is presented. In chapter 2.2, the calibration and validation of the experimental tests, presented in Deliverable D2.1 and an approach for damage prediction has been described. After this calibration, the simulation of the experimental tests showed a very good agreement and also the damage could be mapped satisfactorily.

To investigate different influences, with focus on the section slenderness and the material properties, on the rotation capacity of beams, in chapter 3 700 simulations of I-shaped girders under three-point-bending loading are presented. All simulated beams were able to reach the plastic resistance moment M_{pl} and a certain rotation. The evaluation showed that the unitless rotation capacity is a suitable value to describe the rotation, since it was proportional to absolute values and at the same time comparable. The defined rotation requirement of $R_{req} = 3$ in the background document of EN 1993-1-1 [8] could be reached by most of the beams.

To find a limiting value for beams not suitable for plastic design, many influences have been studied systematically. The main focus was on material properties and the section slenderness. The varied material properties were based on the derivation of flow curves, see Deliverable D1.1. Here, the yield ratio (three levels – lower bound (LB), average values (MW) and upper bound (UB)), the uniform elongation (three levels – LB, MW and UB) and the length of the yield plateau (0.0 %, 2.5 % and 5.0 %) have been varied and combined for different steel grades to define the flow curves. In the first 576 simulations, the two steel grades S500 and S690 were utilised. For each steel grade, 24 flow curves have been applied. The section was varied via the flange and web slenderness c/t_f whereby the flange and web thicknesses were kept constant. For the flange slenderness, three different levels were analysed and four levels for the web slenderness.

The results of the main study showed that the slenderness, especially the web slenderness, has the biggest influence on the rotation capacity. The beams with very slender webs cannot reach large rotations. Looking at the material variation when analysing the individual impact, a higher yield ratio leads to higher rotation capacities. The impact of the uniform elongation is smaller, but a minimum uniform elongation should be guaranteed. With longer yield plateaus the rotation capacity tends to be smaller. The individual influences cannot be described in a general statement on preferred material properties since the combination can lead to opposite effects, which has been shown in additional simulations in chapter 3.1.3. In addition, extreme combinations of flange and web thicknesses leads to low rotations as well as very thin webs or flanges.

In chapter 3.2, additional investigations on imperfections, hybrid sections, length influence, boundary conditions and loading situation, have been conducted.

Regarding imperfections, five different sizes of imperfections (from 0.5 mm to 10 mm) have been implemented. It could be seen that the imperfection size has an influence and with larger imperfection sizes, lower rotations and therefore a lower rotation capacity was achieved. The impact of this is stronger for beams with compact cross sections, which reach, in general, larger rotations than beams with slender cross sections. With regard to the influence of length, it was shown that very short and very long beams reach only small rotations. For longer beams with increasing length, the rotational capacity drops sharply. Another observed phenomenon is, that shorter beams tend to fail due to the occurrence of cracks, whereas longer beams tend to fail due to buckling in the flanges. The variation of the stiffness of the lateral supports shows that up to a specific point, a higher stiffness results in higher rotation capacities. From that certain point onwards, there is no longer a distinct increase of the rotation capacity with increasing stiffness. Stiffeners at the load application and the supports can have a negative influence on the stress concentration, especially on beams with compact cross sections. For slender cross sections, stiffeners are necessary. Also, according to EN 1993-1-1 [8], stiffeners have to be installed at the positions of load application.

Simulation of hybrid beams, where the web is made out of steel with a lower steel grade than the flanges, showed that they reach the same or a higher rotation capacity than the homogenous beams made out of the higher steel grade. At the same time, the hybrid beams reach lower rotation capacities than the homogenous beams made out of the lower steel grade. In general, hybrid beams have advantages regarding the rotation capacity compared to the homogenous high strength beams, but it has to be kept in mind that a hybrid section always leads to a reduced load bearing capacity.

Realizing different loading conditions, a four-point-bending test with compact beams resulted in higher rotation capacities while slender beams show lower rotation capacities. For more equally distributed loads (uniform load, more distanced four-point bending) the M_u/M_{pl} ratio is lower, in some cases even M_{pl} isn't reached, while the rotations are higher. In general, the impact of the loading condition is always related to the cross section.

The general conclusion is that plastic design for high-strength beams (homogenous and hybrid) is in principle possible, since the plastic resistance moment could generally be reached, except for some cases with uniform load and slender cross sections. Nevertheless, additional requirements, especially regarding the cross-section slenderness, are necessary to ensure sufficient rotation capability. Possible requirements are discussed in Deliverable D2.5.

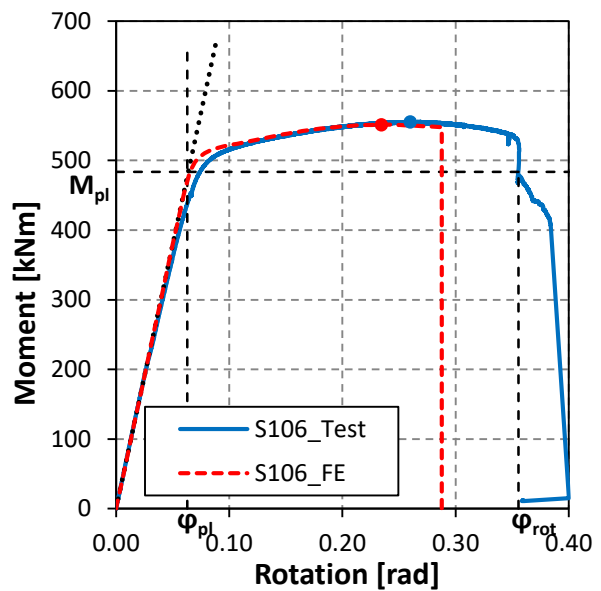
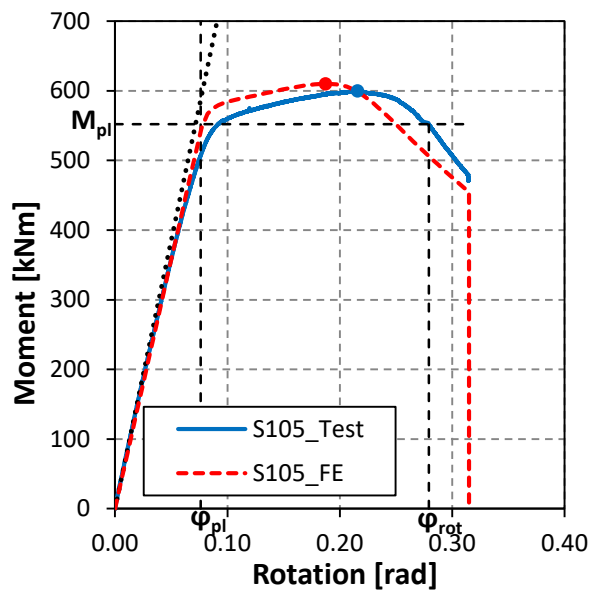
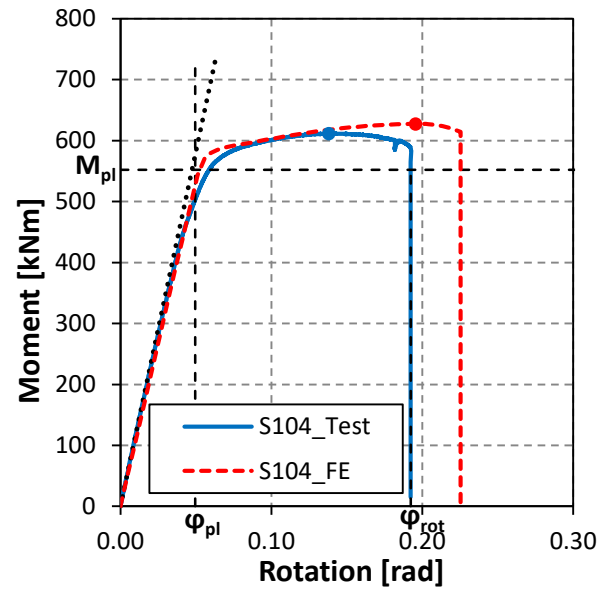
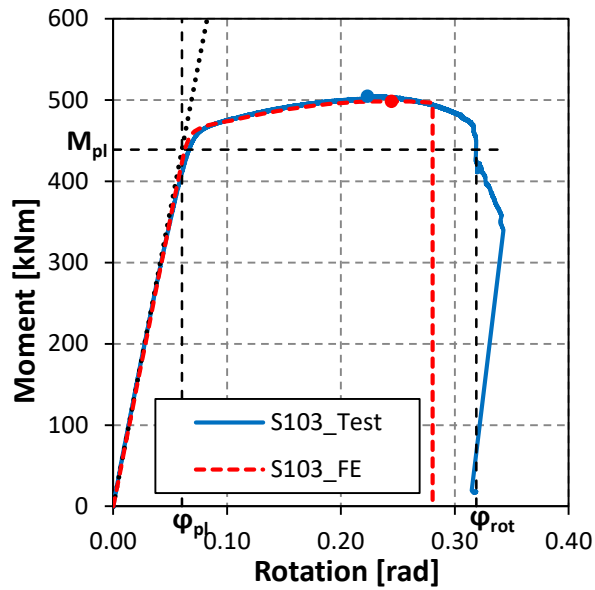
5 REFERENCES

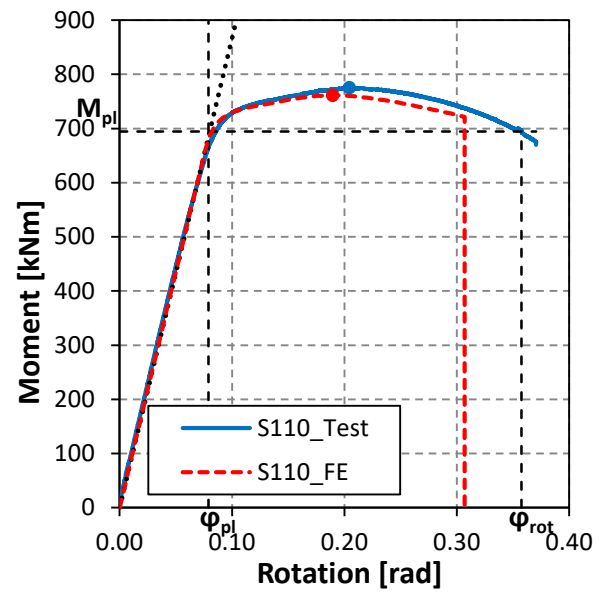
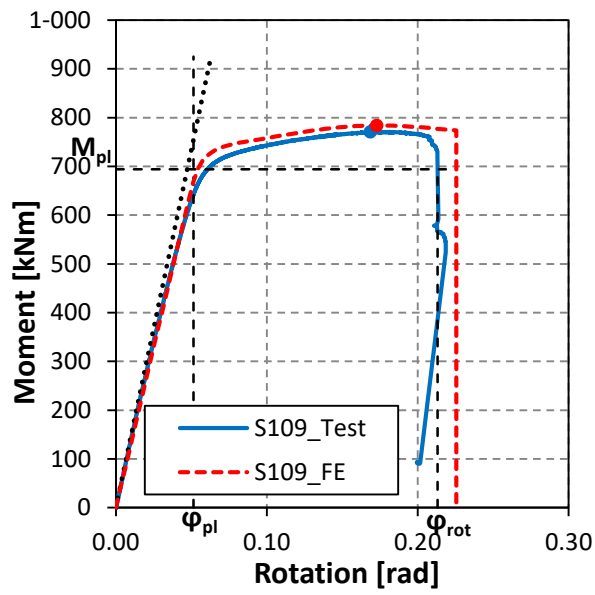
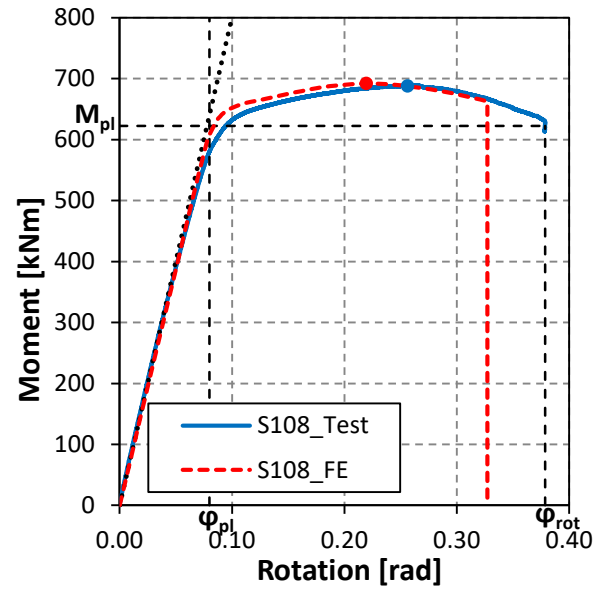
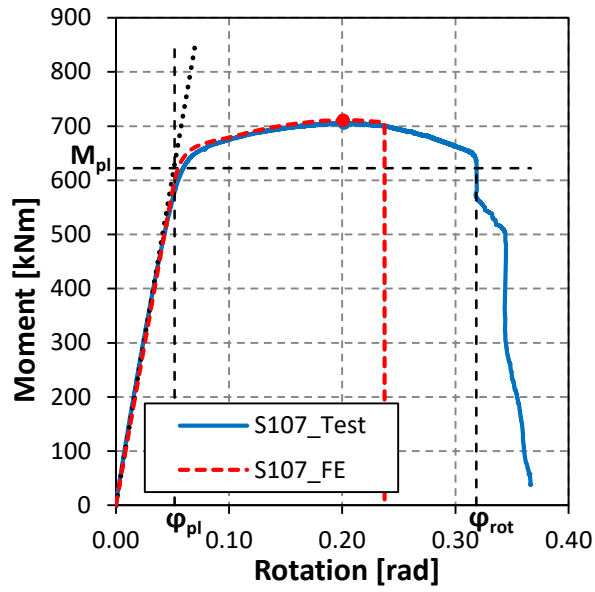
- [1] N. Schillo and M. Feldmann, "The rotational capacity of beams made of high-strength steel," *Structures and Buildings*, no. SB0, pp. 1 - 12, 2016.
- [2] C. Lee, K. Han, C. Uangm, D. Kim and C. K. J. Park, "Flexural Strength and Rotation Capacity of I-Shaped Beams Fabricated from 800-MPa Steel," *Journal of Structural Engineering*, vol. 139, no. 6, pp. 1043 - 1058, 2013.
- [3] P. Ludwik, "Elemente der technologischen Mechanik," Verlag von Julius Springer, Berlin, 1909.
- [4] J. H. Hollomon, "Tensile Deformation," *Transactions of the Metallurgical Society of AIME*, vol. 162, pp. 268 - 290, 1945.
- [5] S. Schaffrath, "Analyse des festigkeitsgesteuerten Tragverhaltens ungeschweißter Stahlbauteile mit Hilfe der Schädigungsmechanik," Dissertation, RWTH Aachen University, Institute of Steel Construction, Aachen, 2018.
- [6] G. R. Johnson and W. H. Cook, "A constitutive model and data for metals subjected to large strains, high strain rates and high temperatures," 1983.
- [7] W. Bleck and M. Feldmann, "Dehnungsbasierte Bemessungskriterien für unbefeuerte Druckbehälter - Demonstration eines erweiterten DBF-Verfahrens (Fosta-Projekt P950)," Aachen, 2014.
- [8] Eurocode 3, Design of steel structures – Part 1-1: General rules and rules for buildings; EN 1993-1-1:2005 + AC:2009.
- [9] Eurocode 3, Design of steel structures – Part 1-12: Additional rules for the extension of EN 1993 up to steel grades S700; EN 1993-1-12:2007 + AC:2009.

6 ANNEX: MOMENT-ROTATION DIAGRAMS

Comparison of moment-rotations diagrams from experimental test and FE after calibration:

Homogenous beams:





Hybrid beams:

